Section 2. Rock Physics

Objective:

1. **Illustrate velocity dependence and sensitivity to elastic constants and environmental factors**
2. **Examine rock-property transforms**
3. **Estimate *P*-wave and *S*-wave velocities when pore-fluid and/or porosity changes**

One of the primary goals of amplitude interpretation is to determine whether a water-saturated rock or a hydrocarbon-saturated rock generated the reflection of interest. In order to accomplish this task, an estimate of the difference in rock properties between the water-saturated and hydrocarbon-saturated states is required. Thus, a few basic relationships of rock physics are necessary. There are both empirical and theoretical relationships between seismic rock properties and elastic constants that will be called upon, as well as wave-propagation models.

The work presented in these notes has drawn heavily from two excellent references. The first is a tutorial article by Castagna et al. (1993): "Rock Physics—The Link Between Rock Properties and AVO Response." The second is a book for those who want detailed solutions to various rock-property transforms but don't want to wade through the messy math. The book is written by Mavko et al. (1998): *The Rock Physics Handbook—Tools for Seismic Analysis in Porous Media*. In addition, the two SEG reprint volumes, *Seismic Acoustic Velocities in Reservoir Rocks*, compiled by Wang and Nur (1992), provide easy access to classic articles on petrophysics.

2A. *P*-waves, *S*-waves, Density, and Poisson's Ratio

Before a theory can be formulated for wave motion in a medium, a relationship between stress and strain is needed. For waves of infinitesimal amplitude, Hooke's empirical law supplies this relationship. The three most commonly used elastic constants to quantitatively describe the strength of a body are the shear (μ), bulk (K), and Young's (E) moduli. The cartoon in Fig.2.A.1 illustrates the hypothetical experiments that measure these elastic constants. In reality, it is difficult to measure the shear modulus (rigidity) as described in the figure and obtain useable results. However, the other two moduli measurements are conducive to lab measurements. As an example, if the bulk modulus of a solid rubber ball were desired, a simple experiment could be conducted. Measure the diameter of the ball and then dive into a deep lake and measure the ball's diameter at the depth of 500 ft (150 m). At 500 ft, the stress (or hydrostatic pressure) is approximately 230 psi (1590 kPa). Knowing the change in stress and the change in volume, the bulk modulus can be computed. Young's modulus is normally measured on thin rodlike specimens.

The experiments described in Fig. 2.A.1 would yield the necessary elastic constants for developing a wave theory if the material were nonporous. For porous material, the

bulk modulus needs to be separated into its components (Fig. 2.A.2). The bulk-modulus components selected in the figure are pertinent to Gassmann's wave propagation theory, which will be introduced later. The three components are the pore-fluid (K_f), matrix-material (K_{ma}), and dry-rock (K_{dry}) bulk moduli. If the pore fluid and matrix material (grains) are known from well-log measurements, their associated bulk moduli can be estimated fairly easily. The dry-rock bulk modulus is a bit more difficult to come by and other relationships will be developed to assist in estimating it.

In Fig. 2.A.3, two of the rock moduli are related to the *P*-wave and *S*-wave velocities. Throughout these notes, the Greek letters α and β will be used interchangeably with V_P and V_S to refer to the *P*-wave (primary or compressional) and *S*-wave (shear) velocities, respectively. While current convention requires that the metric system be employed in geophysical literature, many of the graphs and figures shown in these notes are reproduced from literature and are annotated in the English system. If the bulk moduli of the rock are expressed in gigapascals (GPa) and the density in gm/cc (gm/cm^3), then the resulting velocity is expressed in km/s. The bottom of the figure contains an example with appropriate units for nonporous sandstone.

In order to solve for velocities in the equations of Fig. 2.A.3, the density, ρ, is required. Density is expressed as a function of porosity, ϕ, as shown in Fig. 2.A.4. The bulk density of the rock, ρ, is related to the matrix (grains) and pore-fluid densities. As the bulk density depends on porosity, the fluid density depends on the water saturation, S_W, which is the percentage of the pore space filled with water (brine). What is not indicated is that most rocks are composed of more than one mineral. Thus, the matrix density, ρ_{ma}, needs to be expressed as a volumetric average of the individual mineral densities.

During rock-squeezing experiments in the lab, Poisson's ratio, σ, can also be measured as shown in Fig. 2.A.5 (static measurement). Poisson's ratio, which is Koefoed's lithologic identifier, is simply the negative ratio of the transverse strain to the longitudinal strain. Normally, however, geophysicists express Poisson's ratio as a function of the *P*-wave and *S*-wave velocities (dynamic measurement).

For isotropic media, the value of Poisson's ratio falls between 0.0 and 0.5. The two extremes are useful to examine. When the strained volume is equal to the initial volume, Poisson's ratio is 0.5. This is the case for fluids, which include water, air, and oil. In addition, for the first hundred feet beneath the ocean bottom, Poisson's ratio approaches 0.5 for recent sediments. For those involved in physical modeling experiments, rubber has a Poisson's ratio very close to 0.5. The other extreme occurs when the strained volume has no transverse strain, or as Mike Graul has quoted, "It has zero *fatticity;* it doesn't get fat as you squeeze it vertically." What doesn't get fatter when you squeeze it? A sponge! In exploration geophysics, this occurs in some sense when water is replaced with gas in the pores. Poisson's ratio of the rock always decreases when gas is substituted for water in the pore space.

Substantial differences between the static and dynamic measurements of Poisson's ratio for the same rock are reported in literature. The dynamic Poisson's ratio is normally higher. Wang offered an explanation for these discrepancies. In the dynamic measurements, the propagating waves have strain amplitudes smaller than 10^{-6}, while the static measurements (squeezing in a vise) have strain amplitudes greater than 10^{-3}. That is,

static measurements squeeze the rock more than dynamic methods. Most sedimentary rocks have pores or cracks that are elongated (not spherical) and the propagating waves in the dynamic method do not squeeze these cracks closed. Thus, the rock appears to be stronger (less compressible) than in the situation where the cracks close. In the static method, the cracks close and the rock will appear to have a lower strength. If the experiments are conducted at higher confining pressures so that the cracks are closed at the beginning of the experiment, then static and dynamic measurements of Poisson's ratio approach one another.

A brief preview of the significance of V_P/V_S or Poisson's ratio for discriminating different lithologies is shown in Fig. 2.A.6. This is an idealized plot. At a particular depth, shales tend to have a Poisson's ratio that is larger than that for sands, especially gas-saturated sands. As the depth of investigation becomes shallower, sand and shale Poisson's ratio values move toward 0.5. Also, the sand and shale trends tend to overlap more. Conversely, as the depth of investigation increases, the sand and shale trends tend to separate and have lower Poisson's ratio values—with sand still having a Poisson's ratio lower than shale does. However, with changes of depth, Poisson's ratio for limestone and dolomite does not vary as much as it does for sandstone and shale.

2B. Establishing Regional and Local Rock-Property Trends

Whenever an amplitude anomaly is recognized on a seismic section, the trick is to distinguish what rock-property variation caused the amplitude change. In order to assist in this decision, rules-of-thumb are desired on how velocity is affected by changes in (a) elastic moduli, (b) densities, and (c) various environmental conditions (Fig. 2.B.1). A few of the primary factors affecting velocity are as follows.

Fluid Density—For unconsolidated clastics, pore-fluid variations can significantly change the velocity of the rock. As the pore-fluid density increases, the rock's velocity increases. However, for well-consolidated rocks, porosity variations become more significant than pore-fluid variations for changing the rock's velocity.

Matrix Density—Denser rocks normally have a higher velocity than lighter rocks. Density variations are often the primary component of the reflection coefficient for shallow wet unconsolidated rocks.

Age/Depth—Age, by itself, does not affect the rock's velocity. It is all the other factors that occur over time, such as increased cementation, loss of porosity, compaction, and diagenetic changes. High-velocity rocks tend to have a rapid increase in velocity with depth for the first 3000 ft (900 m) as the micro-cracks close. Then, the velocity increases slowly with depth until the velocity approaches the terminal zero-porosity end member. For unconsolidated rocks, velocity tends to increase linearly with depth, or, more exactly, with increases in effective pressure, which is discussed later.

Water Saturation—As mentioned, if the pore-fluid density increases, the *P*-wave velocity increases. However, this increase in velocity is not necessarily linear with the increase of pore-fluid density. For shallow unconsolidated sediments, a small percentage of gas in the pores significantly decreases the velocity of the rock compared with the water-saturated state. However, once the rock is saturated with 5–10% gas, further gas saturation has little effect on the rock's velocity. Unfortunately, this means that econom-

ic gas reservoirs have almost the same *P*-wave seismic amplitude as a depleted reservoir.

Porosity—There are numerous empirical formulas that log analysts have derived over the years to evaluate a reservoir's porosity in terms of sonic-log traveltime (inverse of velocity). Porosity alters both the density of a rock and its elastic moduli, such that porosity increases yield velocity decreases.

Cementation—Cementation of the grains, which normally increases with age, reduces the porosity and increases the elastic moduli of the rock. Thus cementation increases the velocity of the rock.

Pore Pressure and Overburden Pressure—It is necessary to consider overburden pressure and pore pressure together when analyzing velocity. The overburden pressure on a formation results from the total weight of the rock above it, including the fluid in the rock. If the rock has hydrostatic communication with the surface, then the pore pressure in the rock is equal to the pressure at the base of a column of brine that has a height equal to the formation's depth (hydrostatic pressure). If the overburden pressure is increased while holding the pore pressure constant, the solid matrix will be squeezed closer together and the rock's elastic moduli increase while the density changes little. Similarly, if the pore pressure increases while the overburden pressure remains the same, the pore fluid tends to support more of the overburden and the rock appears weaker and the formation has a lower velocity. This last scenario is an abnormally pressured formation. For our purposes, the overburden pressure minus the pore pressure is called the effective pressure. If the effective pressure is held constant, then no apparent change in velocity is recognized. With an overburden pressure gradient of 1 psi/ft and a pore pressure gradient of 0.47 psi/ft, the effective pressure on the rock increases at 0.53 psi/ft. Thus velocity generally increases with depth.

Shale Content—Normally, the *P*-wave velocity decreases as the shale content is increased. However, this is not always the case. The direction of the velocity change depends on how shale enters the rock: fills the pores, breaches the grain contacts, or replaces part of the skeleton.

From the factors listed above, which one influences velocity the most? Generally, the dominant factors that influence velocity must be determined for an individual area. The different factors are introduced as either filters or variables in trend analyses for regional and local amplitude interpretations. A trend example from the Gulf of Mexico (GOM), which contains essentially unconsolidated clastic sediments, illustrates the concept by filtering the samples based on lithology and the presence of abnormal pressure. Effective pressure is a variable approximated by depth. Velocity and density trends for both sand and shale are desired for quantifying future amplitude interpretations.

Sea-Level Versus Ocean-Bottom Datum

The six well locations illustrated in Fig. 2.B.2 have water depths ranging from 1000 to 7000 ft (300 to 2000 m). Velocity and density histogram trends were developed from these six wells and they are illustrated in Fig. 2.B.3. A histogram trend contains statistical analyses at 500-ft (150-m) depth intervals from a specified datum to approximately 18,000 ft (6000 m) beneath the datum. Velocity and density samples from well-log curves were taken at 1-ft intervals. All lithologies were included and the datum was set at sea level. The vertical line near the maximum-frequency point for each 500-ft his-

togram represents the average value. The small red dot represents a recomputed average after samples more than one standard deviation from the original average were omitted. It is difficult to predict a reliable trend for either velocity or density from the plots in Fig. 2.B.3. The histograms are too disjointed from one depth to the next to be considered reliable. The first impulse is to rerun the data and produce separate histogram trends for sand and shale. However, this is not the primary factor to consider for developing reliable trend curves in this area.

The same six well-log curves were reexamined, but with the depth datum set at ocean bottom (Fig 2.B.4). More continuous and thus reliable trends are produced. Obviously, velocity and density trend curves to be used in amplitude interpretation should be referenced from the ocean bottom. Why?

Effective Pressure

As mentioned earlier, the effective pressure can be a primary factor controlling velocity. The effective pressure is zero in the water column and does not change until sediments are reached. The empirical relationship of effective pressure to in-situ velocity is cartooned in Fig. 2.B.5. The effective pressure, which is approximately the overburden pressure minus the pore pressure, increases linearly until the onset of abnormal pore pressure is reached (at 7500 ft [2300 m] in the figure). The velocity profile also increases linearly to the onset of abnormal pressure. Below the onset of abnormal pore pressure, the fluid in the pores begins to support the overburden rock, and the effective pressure decreases. The two points labeled as V_A on the velocity profile have the same effective pressure and thus have approximately the same in-situ velocity. As a side note, it was this empirical velocity-to-effective-pressure relationship, which can be determined from seismic interval-velocity analyses, that formed the basis of predicting mud-weight programs for drilling engineers (Hottman and Johnson, 1965; Pennebaker, 1968; Dutta and Levin, 1987). This is a very simplistic relationship of interval velocity to effective pressure that needs to be adjusted slightly for actual field conditions.

The expected rock properties beneath the onset of abnormal geopressure depend not only on the effective pressure but also on the environmental reasons for the abnormal pressure. Often, the environmental reasons can be inferred by the change in the shape of the effective pressure curve. In drilling terminology, these changes in effective-pressure curves are called *soft* and *hard* onsets of abnormal geopressure.

A soft onset is illustrated with shale histogram trends from a single well in the southern portion of offshore Louisiana, Vermilion Block 395 (Fig. 2.B.6). At the 6500-ft (2000-m) depth, the onset of abnormal pressure occurred and the mud weight at this depth was gradually increased from 10.3 lbs/gal to 12.4 lbs/gal at the bottom of the hole. The velocity and density values beneath 6500-ft depth are essentially the same as the values at 6500 ft. This indicates that the effective pressure is constant over the depth interval beneath the onset of abnormal pressure. This type of overpressure commonly occurs when the pore fluid trapped by low-permeability shale is squeezed by the weight of newly deposited sediments. This abnormal pressure is referred to as undercompaction or compaction disequilibrium (Bowers, 1995).

A hard onset of abnormal pressure is depicted by the shale histogram trend curves in Fig. 2.B.7. Above the onset of abnormal pressure, the shale rock-property trends are

essentially the same as the soft-onset trend curves, but they differ dramatically below. In the soft onset, the density values beneath the onset have a somewhat predictable trend, but in the hard onset, density values may increase, decrease, or remain constant. Also, the velocity drops significantly when abnormal pressure is reached in the hard-onset case. Bower emphasized the importance of distinguishing this mechanism of overpressure from undercompaction. This overpressure can be generated by fluid expansion such as heating, hydrocarbon maturation, and expulsion/expansion of intergranular water during clay diagenesis. This is an unloading mechanism, and normally the effective pressure decreases more than is predicted from interval velocity. The rock undergoes a plastic and not an elastic rebound.

These significant changes in the velocity and density trends suggest that a horizon map indicating the depth to the onset of abnormal pressure should be incorporated into all amplitude interpretations.

The different mechanisms for generating abnormal geopressure were also correlated to stratigraphy by Verm et al. (1998). The study used over 2700 wells and included GOM regional trend analyses. The maps in Fig. 2.B.8 indicate a strong correlation between the depth to abnormal-pressure onset and the major sand deposits. In the northern portion of the upper map, the onset of abnormal geopressure isn't reached until 14,000 ft (4000 m) in some places, while in the southern portion, the onset occurs as shallow as 2000 ft (600 m). In the upper map, there is a sharp break in the north-south gradient at the 8000-ft (2400-m) contour (red color). This is not surprising because large sand deposits in the northern part of the Gulf provide the pore-fluid conduit for communication to the surface. This is evident in the sand percentage map in the lower portion of the figure that also has the 8000-ft contour overlain. North of the 8000-ft contour line, the expected onset of geopressure is hard and diagenetic changes are responsible for abnormal pressure; while south of the 8000-ft contour, it is mainly soft and caused by undercompaction.

Up to this point, the significance of knowing the effective pressure has been emphasized for unconsolidated sediments. How does lithology affect the velocity and density trend curves?

Velocity and Density Trend Curves for Sand and Shale

In Fig. 2.B.9, sand velocity and density histograms were generated from a 2500-mi^2 (6400-km^2) area in the northern portion of the map shown in Fig. 2.B.8. In this area, the depth to the onset of geopressure was picked for 220 exploration wells. Only data above the onset of geopressure were included in the statistical analyses. There is a surprisingly linear depth trend for both sand velocity and density.

Similar trends for shale were obtained, and the average trend values for the sand and shale properties were fitted with linear equations as shown in Fig. 2.B.10. The best-fit linear trends to the average rock-property values are

$$V_{SAND}\,(\text{ft/s}) = 5530 + .464\,z\,(\text{ft})$$
$$V_{SHALE}\,(\text{ft/s}) = 5820 + .417\,z\,(\text{ft})$$
$$\rho_{SAND}\,(\text{gm/cm}^3) = 2.02 + .0000226\,z\,(\text{ft})$$
$$\rho_{SHALE}\,(\text{gm/cm}^3) = 2.06 + .0000291\,z\,(\text{ft})$$

where z is depth, in feet.

The sand velocity is less than the shale velocity down to approximately 6000-ft (2000-m) depth and then the sand velocity becomes faster than shale velocity. The density contrast between sand and shale increases with depth, with sand being less dense than shale. However, the more important aspect with respect to amplitude interpretation is the reflection coefficient trend as displayed in Fig. 2.B.11. This is based on shale over water-saturated sands. The figure indicates that the acoustic impedance ($\rho\alpha$) of sand is less than shale from the surface to 13,000 ft (4000 m). Even though the velocity of shale is less than sand in the deeper zones, the smaller density values of sand dominate the contrast of the acoustic impedances at depth. The next logical step would be to investigate these relationships below the onset of abnormal geopressure. However, this is a more difficult problem.

In Fig. 2.B.12, a shale-velocity histogram trend for a single well that encounters abnormal pressure is illustrated. This well is from the deep-water area of GOM. There are several interesting points. First, end-member lithologies were analyzed in order to establish upper and lower bounds for the shale properties. The velocity trends for two end-member shale lithologies are shown. The lower-velocity bound is the clay-rich shale trend in abnormal pressure. This is essentially the minimum shale velocity in abnormal pressure. The other end-member is the shale normal-compaction curve for samples above the onset of geopressure. Above the onset of abnormal pressure in the figure, the trend from the single-well histogram is near the normal-compaction trend curve. In abnormal pressure, the shale velocity from the single well falls between the two end-member curves.

Another point is that shale-over-shale reflection amplitudes can be larger than shale-over-sand amplitudes in some areas. This is indicated on the histogram in Fig. 2.B.12 by the large velocity spread within a single 500-ft (150-m) depth interval. The figure indicates that the reflection amplitude from the velocity contrast between the shales within one 500-ft interval could be as large as 0.086. This number is several times larger than the shale-over-sand reflection amplitudes shown in Fig. 2.B.11. In the GOM, areas that are near the 8000-ft (2400-m) contour of abnormal geopressure (Fig. 2.B.8, by Verm et al.) exhibit large shale-over-shale reflections.

For unconsolidated rocks, velocity values are strongly correlated to effective pressure. The effective pressure is related to depth until the onset of abnormal pressure is reached. Beneath the onset of abnormal pressure, the effective pressure can be strongly correlated to the effective pressure just above the onset depth. This suggests that only local trend curves in abnormal pressure should be applied in amplitude interpretation, not regional ones where the onset of abnormal pressure varies significantly with depth.

In summary, in order to determine the significance of amplitude anomalies, local calibrations of rules-of-thumb are needed. These include quantitative rock-property measurements as a function of the anticipated lithologies and environmental conditions. Not only are average trends required, but we also need variations of the rock properties within short depth intervals. As illustrated above, linear-with-depth trends appear to fit unconsolidated rocks in the GOM. However, this is an isolated example and the trend values are applicable in this one area. Petrophysicists have reported numerous other empirical relationships, and these will now be examined.

2C. Empirical Relationships between Velocity and Density

Fig. 2.C.1 suggests several reasons for wanting empirical velocity-density relationships. The applications range from generating missing well-log curves and quality-controlling logs in questionable zones, to explaining anomalous seismic amplitudes. With the advent of AVO, new empirical transforms have been advocated for predicting *S*-wave velocity from other logs and also for predicting velocity changes when the pore-fluid is varied. However, as a warning beforehand, many of the transforms to be discussed are not only highly dependent on lithology, but are also very dependent on local conditions and shouldn't be extrapolated to other areas without recalibration.

Gardner's Velocity-Density Transform

At the 38th Annual International SEG Meeting in Denver (1968), Gardner et al. presented petrophysical principles for distinguishing gas-saturated sands from water-saturated sands using the seismic method. Gardner et al.'s published results (1974) were similar to Domenico's (1974). These authors had an impact on how pore-fluid content is analyzed from seismic data.

Gardner et al.'s velocity-density crossplots (1974) for various lithologies along with the average transform of $\rho = .23V^{.25}$ (gm/cm^3 and ft/s) are shown in Fig. 2.C.2. This average transform is a best-fit curve for all lithologies and was not intended for application to individual lithologies. Overall, however, the average transform fits the velocity-density pairs with only a couple of outliers. Salt is too light for its velocity, and anhydrite is too heavy. Gardner et al.'s average transform falls between the sand and shale trend lines.

Castagna (1993) extended Gardner's work by developing velocity-density transforms for lithologies plotted in Fig. 2.C.2. The revised transforms in gm/cm^3 and ft/s are

Sand:	$\rho = .200\ V_P^{.261}$
Shale:	$\rho = .204\ V_P^{.265}$
Limestone:	$\rho = .243\ V_P^{.225}$
Dolomite:	$\rho = .226\ V_P^{.243}$
Anhydrite:	$\rho = .600\ V_P^{.160}$

In order to emphasize the importance of developing individual lithologic transforms, Castagna overplotted his best-fit sand and shale transforms on a set of well-log and laboratory measurements of velocity-density pairs (Fig. 2.C.3). As has been observed by many geophysicists, the average transform, $\rho = .23V^{.25}$, overestimates the density of sand and underestimates the density of shale. With the revised transforms, there is a better correlation to the raw data.

However, when Castagna's transforms for sand and shale are applied to the data sets previously displayed in Fig. 2.B.10, the correlation is not satisfactory (Fig. 2.C.4). Using the data themselves, the log-log best fits are shown in Fig. 2.C.4. Castagna's shale transform and the transform derived from the data themselves yield approximately the same results. However, the significant differences between the two sand transforms highlights a statement that Mavko et al. (1998) frequently note in their book: "These relations are empirical and thus strictly speaking they apply only to the set of rocks studied."

Wyllie's Velocity-Porosity Transform

In 1956 and in subsequent publications (1958 and 1963), Wyllie et al. proposed the empirical relationship between velocity and porosity for brine-filled porous media of

$$1/V = (1-\phi)/V_{ma} + \phi/V_{fl} \quad [1]$$

where V = velocity of total rock, V_{ma} = velocity of the matrix material, V_{fl} = velocity of pore fluid and ϕ = porosity. This is often expressed in terms of interval traveltime (μs/ft) as

$$\Delta t = (1-\phi)\,\Delta t_{ma} + \phi\,\Delta t_{fl} \quad [2]$$

where the Δt's represent the respective traveltimes (Fig. 2.C.5). When expressed in interval traveltimes, Wyllie's equation represents the total time it takes to pass through the porous material and matrix material individually. This heuristic interpretation is illustrated in the figure.

Obviously, the variable Δt_{ma} is dependent on lithology. Commonly used values for Δt_{ma} (μs/ft) as reported by Schlumberger are

Sandstone	55.5 or 51.0
Limestone	47.5
Dolomite	43.5
Anhydrite	50.0
Salt	67.0
Brine	189.0 (Δt_{fl})

When applying Wyllie's transform, there are numerous assumptions and conditions that should be considered. Notwithstanding this, Wyllie's transform is still very popular. In order to apply Wyllie's transform when an assumption has been violated, numerous authors have suggested empirical corrections for shaliness, mixed lithologies, hydrocarbon saturation, etc. A couple of examples will demonstrate these limitations and corrections.

In Fig.2.C.6, velocity-density pairs from porous limestone reefs were crossplotted and three empirical transforms were overplotted. The limestone is considered to be consolidated material. Two expressions are similar to Wyllie's suggested transform. The transform with a Δt_{ma} of 47.5 is the commonly used equation for limestone and the one with 46.6 is an "eyeball" adjustment to better fit the data. The third equation is a linear-fit of velocity to porosity. The porosity values ranged from 0% to 44%. All three expressions provide adequate transformations between velocity and density.

However, a satisfactory correlation does not exist for lower-velocity unconsolidated rocks. Using the measured velocity-density pairs from Fig. 2.B.10 again, the time-average curve for sandstone is overplotted in Fig. 2.C.7. The red curve represents the time-average equation with commonly used values of 55 and 189 μs/ft for the matrix and fluid traveltimes, respectively. The results are poor. A least-squares fit from the actual

data set yields matrix and pore-fluid traveltimes of −22.3 and 467, respectively. This is plotted as the blue curve. The blue curve provides an adequate fit for densities below 2.25 gm/cm^3 but then the fit begins to diverge quickly for larger density values. Obviously, with a negative traveltime of −22.3 μs/ft for the matrix material, no physical meaning can be associated with the best-fit traveltimes. Matrix materials don't have negative velocities.

As mentioned, there are several assumptions and limitations that are inherent in the application of Wyllie's time-average equation (Mavko et al., 1998). A few are:

- Use for brine pore fluid,
- Use for rocks beneath 8700-ft (2700-m) depth (equivalent to 30 MPa if an effective pressure gradient of 0.5 psi/ft is assumed),
- Use for consolidated cemented rocks, and
- Use for intermediate porosity.

In shallow uncompacted sands, an adjustment to the porosity term in Wyllie's time-average equation has been suggested to make the transform more accurate. The original porosity term, ϕ, is replaced with $[t_{SH}/100]\phi$. When estimating the porosity of sand, any time the neighboring shale sonic traveltime is over 100, apply the adjustment with t_{SH} representing the shale traveltime. This adjustment lowers the value of the estimated porosity.

Raymer-Hunt-Gardner's (R-H-G) Velocity-Porosity Transform

In an effort to improve upon Wyllie's empirical time-average equation, Raymer et al. (1980) proposed the following velocity-porosity relationships (from Mavko et al., 1998):

$$V = (1-\phi)^2 V_{ma} + \phi V_{fl} \qquad \phi < 37\% \qquad [3]$$

$$1/V = (0.47 - \phi)/(.1\ V_{37}) + (\phi - .37)/(.1\ V_{47}) \qquad 37 < \phi < 47\% \qquad [4]$$

$$1/\rho V^2 = (1-\phi)/(\rho_{ma} V_{ma}^2) + \phi/(\rho_{fl} V_{fl}^2) \qquad \phi > 47\% \qquad [5]$$

where V_{37} is calculated from the low-porosity equation at $\phi = .37$ and V_{47} is calculated from the high-porosity equation at $\phi = .47$.

Once again, the data set in Fig. 2.B.10 was used to analyze the R-H-G equation. The results are shown in Fig. 2.C. 8. With the suggested values of 18,182 ft (5546 m)/s and 5291 ft (1614 m)/s for V_{ma} and V_{fl} respectively, the R-H-G match to the measured velocity-density pairs is unacceptable. Thus, even though the R-H-G transform was developed to better estimate lower-porosity values from sonic readings, it is still not adequate for all areas.

A least-squares fit from the data themselves for V_{ma} and V_{fl} yields acceptable correlation between velocity and density. However, once again, no physical meaning should be attached to the two variables. In fact from the data themselves, the influence of the pore-fluid was in the negative direction with $V_{fl} = -5000$ ft (1525 m)/s.

In summary, log analysts have provided the industry with numerous velocity-density (velocity-porosity) transforms that have inherent limitations and assumptions. In the above, three different mathematical expressions were examined. Often, constants for the matrix and pore-fluid properties are selected to ensure that the transform equations are realistic at the end-member porosity values of 0% and 100%. Additional mathematical forms with higher-order porosity terms are often entertained. However, for seismic modeling, it appears that mathematical predictions based on fitting regional and local trend analyses would be more robust. To apply any of the transforms blindly is dangerous. For instance, if a density curve has to be estimated for forward modeling, the 1-D synthetic might match quite adequately with the estimated density curve because of the overriding influence of in-situ velocity. However, the velocity estimate obtained during a pore-fluid substitution is sensitive to the original porosity value. Errors made in estimating the in-situ density curve will then visibly affect pore-fluid substitution AVO modeling.

Han's Velocity-Porosity-Clay Volume Transform

Empirical transforms are often valuable not only for the direct estimates of a rock-property value, but for the functional relationship they provide between the variables. For instance, they may provide insight into the relative changes in *P*-wave and *S*-wave velocities as the porosity content and clay content are varied.

Han (1986) and Han et al. (1986) developed empirical relationships among velocity, porosity, and clay content, C, using ultrasonic measurements on 75 well-consolidated sandstones. Measurements were conducted with variations of effective pressure and water saturation. A few results from the minimum and maximum effective-pressure measurements will be examined. Han's transforms are

Clean sandstones:

40MPa $V_P = 6.08 - 8.06\phi$ $V_S = 4.06 - 6.28\phi$ [6]

Shaly Sandstones:

40MPa $V_P = 5.59 - 6.93\phi - 2.18C$ $V_S = 3.52 - 4.91\phi - 1.89C$ [7]

5MPa $V_P = 5.26 - 7.08\phi - 2.02C$ $V_S = 3.16 - 4.77\phi - 1.64C$ [8]

With the conversion of 1MPa = 145 psi and an effective pressure gradient ≈ 0.5 psi/ft, the measurements at 40 MPa and 5 MPa correspond to approximate depths of 12000 ft and 1500 ft, respectively.

The relationships of porosity and clay content to velocity and Poisson's ratio are shown in the graphs of Fig. 2.C.9. In the crossplots in the left of Fig. 2.C.9, the porosity was set to 15% as the clay volume, C, varied. In the crossplots in the right of Fig. 2.C.9, the clay volume was set to 20% as the porosity varied. For these well-consolidated sandstones, a few observations can be drawn.

- Velocity variations as a function of depth are smaller for well-consolidated sandstones than for unconsolidated sands (as shown in Fig. 2.B.10).

- As the percentage of porosity or clay volume increases, the velocity decreases about 2.5 times more for porosity than for clay volume.
- As the percentage of porosity or clay volume increases, Poisson's ratio increases.
- Poisson's ratio decreases with depth.

Han noted an interesting petrophysical property for clean sandstones. This resulted by subdividing the data set. The clean-sandstone equations were derived using a subset of samples, with only 10 clean-sandstone samples. However, all samples were used, including the clean sandstones, when the shaly-sandstone equations were derived. The clean-sandstone equations listed above have no clay component. However, clean-sandstone velocities can also be estimated with the shaly-sandstone equation by setting C=0. The results of computing clean-sandstone velocities from the two equations at an effective pressure of 40 MPa are depicted in Fig. 2.C.10.

There are significant differences in the estimated Poisson's ratio values depending on which equation was used. Han et al. noted the petrophysical significance of this by stating "... a very small amount of clay (1% or a few percent of volume fraction) significantly reduces the elastic moduli of sandstones." The reduction is more for the shear modulus than for the bulk modulus.

In a typical clastic basin, most sands contain a small amount of clay. Thus, when a clean sand is encountered, there is a significant reduction in its Poisson's ratio when compared with surrounding shaly sands. This Poisson's ratio reduction can make clean, water-saturated sand appear as if it is hydrocarbon-saturated during an AVO interpretation.

Castagna's V_P-to-V_S Transforms

Pickett (1963) introduced the concept that V_P/V_S ratios could be used for identifying lithology. This concept didn't receive much attention until Ostrander (1982) verified that V_P/V_S ratios could be inferred from seismic data. In 1985, Castagna et al. published additional laboratory and in-situ measurements of V_P/V_S ratios. An interesting result that came from this article was the robustness of the V_P/V_S ratio for clastic silicate rocks composed primarily of clay- or silt-sized particles. Castagna et al. called this relationship the mudrock line and expressed the velocity relationship as

$$V_P = 1.16V_S + 1.36 \qquad [9]$$

where the velocities are expressed in km/s.

Greenberg and Castagna (1992) published additional V_P-to-V_S transforms in their work on pore-fluid substitution techniques, based on the Gassmann equation. They assumed that a conventional suite of well-log curves would normally be available for modeling. As they noted, however, when no in-situ V_S information is available, additional empirical information is needed to solve Gassmann's equation for the fluid-substitution problem. Greenberg and Castagna provided this needed information in the

form of V_P-to-V_S transforms for various water-saturated lithologies. Their transforms, in km/s, are:

Sandstone:	$V_S = -0.856 + 0.804\ V_P$	[10]
Limestone:	$V_S = -1.030 + 1.017\ V_P - 0.055\ V_P^2$	[11]
Dolomite:	$V_S = -0.078 + 0.583\ V_P$	[12]
Shale:	$V_S = -0.867 + 0.770\ V_P$	[13]

To convert the above equations to ft/s, multiply the V_P^2 term by (1/3280), the V_P term by 1, and the constant by 3280. These transforms are graphed in Fig. 2.C.11. In addition, Gassmann's estimate of Poisson's ratio for a gas-saturated sandstone is plotted. Note, however, that the velocity of the gas-saturated sand *cannot* be obtained from this plot. The *x*-axis is based on the water-saturated sand velocity. An example will demonstrate the proper reading of this graph. A water-saturated sand that has a velocity of 12,000 ft/s has a Poisson's ratio of approximately 0.275 and when this sand is fluid substituted with gas, its Poisson's ratio lowers to 0.200, the value vertically beneath the water-saturated Poisson's ratio.

The reason for plotting Poisson's ratio against V_P rather than V_S can be found in Fig. 1.C.3. The AVO equation in this figure is

$$RC(\theta) \approx \frac{(\rho\alpha)_2 - (\rho\alpha)_1}{(\rho\alpha)_2 + (\rho\alpha)_1} \cos^2(\theta) + \frac{\sigma_2 - \sigma_1}{(1-\sigma_{avg})^2} \sin^2(\theta). \quad [14]$$

This equation indicates that the amplitude at non-zero incident angles will be a function of the lower medium's Poisson's ratio minus the upper's. Thus, Poisson's ratio appears to be a rock property that links directly to AVO.

There are other interesting observations that are depicted in Fig. 2.C.11.

- The difference between Poisson's ratio for water-saturated sand and for shale increases as velocity increases.
- Poisson's ratios for water-saturated sand and for shale approach each other for low-velocity unconsolidated sediments.
- The difference between Poisson's ratio for gas-saturated and for water-saturated sands decreases as velocity increases.
- Above 11000 ft/s, Poisson's ratio for limestone is essentially constant.
- Poisson's ratio for dolomite is essentially constant.

As a warning, the gas-saturated Poisson's ratio curve in Fig. 2.C.11 was based on a density function derived from the expression, $\rho = .200\ V_P^{.261}$. The gas-saturated velocity that is estimated for a specific in-situ wet sand is sensitive to porosity. In short, density-velocity relationships or trends should be derived locally for the creation of the gas-saturated Poisson's ratio curve. The V_P-to-V_S transforms are more robust than velocity-density transforms (Castagna, 2000, personal communication).

2D. Relationships for Bulk Moduli

Just outside Golden, Colorado, the highway department has built a series of walking paths alongside a large road cut that traverses numerous outcropping formations. An observer will notice that within a particular formation, the rock properties vary significantly with respect to porosity, grain size, fracture patterns, rock types, etc. Any geophysicist who has taken the time to view these outcrops has to marvel at the simplistic averaging that is employed in the seismic method. Do we really assign just one velocity and one density to represent a formation's properties? In essence, yes. Effective-medium theory is applied.

An effective medium is assumed to be macroscopically homogeneous and isotropic, so that only two elastic constants are necessary to define the entire medium or formation. The key is to define an adequate mixing model of the composite material. Wang and Nur (1992) provide an excellent tutorial on the various petrophysical models and theories that are commonly applied by geophysicists. In a sense, the Wyllie and R-H-G transforms are effective-medium theories that incorporate a mixing model in the choice of V_{ma} and V_{fl}.

But why are we examining effective-medium theories? One of the primary reasons is to estimate the changes in V_P and V_S for different pore-fluid saturants (Fig. 2. D.1). This process is often called fluid-replacement or fluid-substitution modeling. Most rocks are composed of at least two different materials: the matrix or grain material and the pore-fluid material. The example in the figure has two mineral components, quartz sand and shale. In addition, the pore fluid will have two components for the hydrocarbon state.

It was noted earlier that the velocities of the rock depend upon the bulk and shear moduli of the total rock, along with the density. When the pore-fluid is changed in a rock, the dry-rock bulk modulus (K_{dry}) and mineral bulk modulus (K_{ma}) normally remain the same. Only the fluid properties change. How does the total or effective moduli (K) of the rock change when only one component (pore-fluid) is changed? In order to answer this question, methods to estimate K_{ma}, K_{dry} and K_{fl} are needed.

In this section, I discuss several effective-medium theories that average the elastic constants rather than the composite velocities of the medium. In addition, empirical relationships between the individual bulk moduli (K_{ma}, K_{dry} and K_{fl}) will be examined.

Voigt, Reuss, and Hill's (V-R-H) Moduli Models—K_{ma} Estimate

In Fig. 2.D.2, V_P and V_S are expressed as a function of two effective moduli, K_{eff} and μ_{eff}. These moduli represent the macroscopic scale of the material. In the late 1920s, Voigt (1928) and Reuss (1929) proposed two different mixing laws to compute these effective moduli from the individual moduli of the composite material. Reuss's method provided the lower limit for the effective moduli, while Voigt's provided the upper limit. However, Hill (1952) suggested that an average taken from the Voigt and Reuss models would yield a better estimate.

Wang and Nur (1992) tested the V-R-H model with laboratory data, and their results are shown in Fig. 2.D.3. As noted, the Voigt and Reuss models place upper and lower bounds on the effective moduli of the composite material. The Hill model comes

close to matching the best-fit curve for the bulk modulus, but the Hill model should not be used to estimate the shear moduli. They also note that the V-R-H model should not be used for gas-saturated rocks. These last two constraints limit the direct application of the V-R-H model for predicting V_P and V_S from a volumetric analysis of a rock. In short, the V-R-H model is used to estimate the effective bulk modulus of the mineral (grain) components, K_{ma}, not the total bulk modulus.

In order to estimate the effective bulk modulus of the various minerals with the V-R-H model, the volumetric percentage of each mineral and the porosity must be known. In addition, the bulk moduli of the minerals and pore fluid are required. Mineral bulk moduli and density values (at porosity = 0%) from a list compiled by Mavko et al. (1998) and other authors are expressed in GPa and gm/cm^3 as:

Mineral	*Bulk Modulus*	*Density*
Clay	25	2.55
Coal	5	1.40
Quartz	40	2.65
Halite salt	25	2.16
Calcite	71	2.71
Anhydrite	54	2.98
Dolomite	80	2.87
Plagioclase feldspar	76	2.63

Wood's Pore-Fluid Modulus Model—K_{fl} Estimate

There are two scenarios where Wood's model (1955) is of use to the geoscientist: for estimating the effective bulk modulus of pore-fluid K_{fl} and for estimating the effective bulk modulus of shallow-marine sediments that are essentially in suspension. Wood's velocity equation (Fig. 2.D.4) employs the Reuss model to compute the effective bulk modulus and assigns a value of zero to the shear modulus.

Three suspension models are given at the bottom of the figure. The first model has both the porosity and water saturation equal to one. This is the trivial case for an all-water model where $K_R = K_{WATER}$. The second model has porosity = 1 and the water saturation is a variable. This is designed for determining the pore-fluid bulk modulus, K_{fl}, for a mixture of hydrocarbons and water. The last model determines the bulk modulus for ocean-bottom sediments. That is, $K_R = K$, the total bulk modulus.

Fig. 2.D.5 illustrates two applications of Wood's equation. The left graph represents an ocean-bottom sediment model. The composite material has quartz grains and water with $S_W = 1$. The densities and bulk moduli are listed under the graph. At $\phi = 0.0$, the composite material is all quartz. For porosity values between 50% and 100%, the model represents ocean-bottom sediments. The velocity associated with this porosity range is essentially that of water. On the right graph, a pore-fluid mixture of gas and water is modeled as a function of water saturation (S_W). The most obvious feature on this plot is that a little bit of gas (S_W = 95%) immediately drops both the velocity and effective bulk modulus of the pore fluid. Once 5% gas has been introduced into the pore volume, there is little change in the pore-fluid bulk modulus or pore-fluid veloci-

ty. Obviously, this pore-fluid effect relates to the elastic properties of sands that have partial gas saturation.

One difficulty with Wood's model is that the shear modulus and thus V_S are assumed to be zero. While the V_P predicted from Wood's model for shallow ocean-bottom sediments is fairly accurate when compared with actual field experiments, measured V_S is not zero. If V_S were zero for suspended loads, then ocean-bottom horizontal phones would have difficulty recording converted *PS* waves. Hamilton (1979) published measured V_S values for ocean-bottom (OB) sediments and his results indicate a change in the V_S gradient at approximately 60 m beneath the ocean bottom. Marfurt (2000, personal communication) emphasized the importance of this V_S gradient in separating *PP* from *PS* wavefields in OB multicomponent data.

The effective pressure for shallow OB sediments is also akin to highly overpressured sediments. Here, pore pressure approaches the overburden pressure (small effective pressure) and the *P*-wave velocity decreases but the *S*-wave velocity decreases more dramatically: same as with shallow OB sediments. This rapid decrease in V_S was emphasized to the author while examining an unpublished walkaway *VSP*. The *PP* waves from the *VSP* were very poor for detailing structure beneath the onset of abnormal pressure. However, the converted *PS* waves clearly imaged the reservoir and fault planes.

Batzle and Wang's Estimation of Pore-Fluid Properties

In order to apply Wood's equation for estimating the bulk modulus of the pore fluid, the bulk moduli of water and hydrocarbons are required. The values listed at the bottom of Fig. 2.D.5 were taken from Domenico's (1974) graphs shown in Fig. 2.D.6 for a depth of 5000 ft (1500 m). While the density and bulk-moduli curves for oil and brine appear to be near one another in Figure 2.D.6, an increase in the gas-oil ratio will move the oil curves quickly toward methane values.

A more detailed and recommended approach for determining the pore-fluid bulk moduli and density has been given by Batzle and Wang (1992). Current pore-fluid modeling programs implement some version of their algorithms. In their procedure, the bulk moduli and density of a pore-fluid component are expressed in terms of pore temperature, pressure, salinity, GOR, API number, and specific gas gravity. After the bulk moduli of the pore-fluid components are determined, the effective bulk modulus of the total fluid is determined using Wood's equation.

Biot's Coefficient

In Fig. 2.A.2, the bulk modulus of the total rock K (effective rock bulk modulus) was shown to be dependent on three bulk moduli: the pore-fluid bulk modulus, K_{fl}; the matrix bulk modulus, K_{ma}; and, the dry-rock bulk modulus, K_{dry}. As has been discussed, two of these bulk moduli, K_{fl} and K_{ma}, can be estimated if the volumetric mineral and pore-fluid components of the rock are known. The third, K_{dry}, is elusive and yet, is a very important component for validating amplitude interpretations and providing sensitivity analyses (the what-ifs). Thus, numerous petrophysicists have developed empirical approximations to estimate this property based on other known prop-

erties of the rock. Many of the techniques are related to Biot's coefficient as expressed in Fig. 2.D.7.

Biot's coefficient, B, is a function of K_{ma}, which can be estimated, and K_{dry}, the desired dry-rock bulk modulus. B values range from 0 (well-consolidated sediments) to 1 (unconsolidated sediments and suspended loads). One of the most popular experimental approaches has been to approximate B as a function of porosity. The following have been suggested.

1. Geertsma (1961) $B = 1 - [1 + 50\phi]^{-1}$ [15]
2. Krief et al. (1990) $B = 1 - [1 - \phi]^{[3/(1-\phi)]}$ [16]
3. Nur et al. (1991) $B = \phi/\phi_{crit} \quad \phi < \phi_{crit}$ [17]
   $B = 1 \quad \phi \geq \phi_{crit}$ [18]

where (Mavko et al., 1998):

Material	*Critical porosity* (ϕ_{crit})
Sandstone	40%
Limestone	60%
Dolomite	40%
Pumice	80%
Chalk	65%

4. Polynomial expansion of $K_{dry}/K_{ma} = a_0 + a_1\,(\phi/\phi_{crit}) + a_2\,(\phi/\phi_{crit})^2$ [19]
   leads to $B = 2(\phi/\phi_{crit}) - (\phi/\phi_{crit})^2$ [20]
   from the initial conditions of:

$K_{dry}/K_{ma} = 1$ at $(\phi/\phi_{crit}) = 0$
$K_{dry}/K_{ma} = 0$ at $(\phi/\phi_{crit}) = 1$
$d(K_{dry}/K_{ma})/d(\phi/\phi_{crit}) = 0$ at $(\phi/\phi_{crit}) = 1$

The Krief model incorporates the H-R-G relationship. The Nur model is based on empirical observations from laboratory measurements and the introduction of the critical porosity term.

With $\phi_{crit} = 50\%$ for the polynomial equation and $\phi_{crit} = 40\%$ for Nur's, the above four expressions for Biot's coefficient are graphed in Fig. 2.D.8 as a function of porosity. As depicted in the figure, the Krief, Nur, and polynomial equations yield similar results.

With methods to estimate K_{ma} and K_{fl} developed, pore-fluid substitution techniques and predictions of V_S are possible. The significance of the Biot coefficient will also become evident in later discussions.

2E. Wave Propagation Theories

Of the many wave-propagation theories in the geophysical literature, Gassmann's (1951) has been the most widely applied by geophysicists (Fig 2.E.1). Gassmann's equation is popular because of the ease in providing values for the parameters in his equation. Basically, Gassmann derived an equation that relates the effective bulk-modulus of a fluid-saturated rock to that of the bulk moduli of the matrix material (K_{ma}), the frame (K_{dry}), pore fluid (K_{fl}) and porosity (ϕ). Methods to estimate K_{ma} and K_{fl} were discussed in the previous section.

Biot's (1956a) theory is an extension of Gassmann's (1951) theory. Biot included fluid viscosity and the fact that the pore fluid could move relative to the frame. With viscosity, Biot's model exhibited attenuation and the possibility of having two *P*-waves propagating at different velocities through the medium. However, values for the parameters required in Biot's equation are more difficult to derive, and quite frankly more difficult to understand intuitively.

The Kuster-Toksöz (1974) theory is a low-porosity model that provides options to change the size, shape and distribution of cracks in the rock. Xu and White (1995) provided a technique to model mixtures of clay and sand that incorporates Gassmann, Wyllie, and Kuster-Toksöz theories.

If only the conventional well-log suite of gamma, SP, resistivity, neutron, density, and *P*-wave sonic curves are available, none of the theoretical models mentioned above have enough information to estimate V_S. Thus, geophysicists need additional empirical models. The fact that Gassmann's equation only requires one additional piece of information and correlates fairly accurately to field measurements makes it an obvious choice. In addition, the empirical models selected to provide the additional information needed to solve Gassmann's equation can be adjusted regionally.

Gassmann's Equation

Gassmann's equation can be separated into two components: the dry rock and fluid (Fig. 2.E.2). The dry-rock bulk moduli are a function of the frame and are independent of the pore-fluid properties. Thus, K_{dry} and μ_{dry} remain the same for computing V_P when the pore space has hydrocarbons or is totally water saturated. The dry-rock moduli are not independent of porosity, so if porosity is changed, then new K_{dry} and μ_{dry} are required. There are two equations and nine variables listed in the figure.

Let's start with a typical scenario of having a suite of conventional well-log curves. Now, an estimate of V_P and V_S is desired when the pore-fluid is changed from the in-situ condition. All that is necessary is to plug in values for the variables listed in Gassmann's equation. But as Fig. 2.E.3 questions: "What's known and what's unknown?" Starting with the in-situ well-log curves, the *P*-wave velocity and density can be measured. Likewise, an estimate of the porosity can be made. The bulk modulus of the matrix material, K_{ma}, can be computed from numerous mixing laws such as the V-R-H. However, a volumetric analysis and the mineral bulk-moduli values are required. An additional component of the volumetric analysis is the in-situ description of the pore-fluid components. From this, the pore-fluid bulk moduli, K_{fl}, can be estimated using the Batzle-Wang algorithms or taken from graphs such as Domenico's. In short, this leaves three unknown parameters, K_{dry}, μ_{dry}, and the desired V_S, but only two equations. This is why empirical models, such as the ones previously discussed, are called upon. Fig. 2.E.4 summarizes a few choices. Additional empirical relationships besides those listed in Fig. 2.E.4 are suggested by Mavko et al. (1998).

A popular choice is to estimate V_S using the known volumetric analyses and V_P. Once this is done, then K_{dry} and μ_{dry} can be determined. Although these V_P-to-V_S transforms are based on water-saturated rocks, Greenberg and Castagna (1992), provide an iterative solution when the in-situ pore space contains hydrocarbons.

Greenberg and Castagna also emphasized the importance of recalibrating the V_P-to-V_S coefficients for the local area when a measured V_S is available.

Once the variables in Gassmann's equation are solved for the in-situ case, the fluid substitution case is straightforward. With a description of the pore fluid to be substituted, a new density and bulk modulus, K_{fl}, are computed. Then estimates of V_P and V_S with the new pore fluid are made.

The same procedure is followed if another choice besides the Greenberg and Castagna equation from Fig. 2.E.4 is selected. For consolidated rocks, empirical relationships based on Biot's coefficient are often chosen. These relationships should also be calibrated to local areas when possible. The previous section describes four different relationships of the Biot coefficient versus porosity.

Gregory (1977) suggested using a value of 0.10 for the dry-rock Poisson's ratio as the additional seed for inverting Gassmann's equation for unconsolidated sands. He noted that σ_{dry} is independent of pressure, and the calculated V_P was not very sensitive to this estimate. In an effort to extend Gregory's relationship to shale and limestone, Hilterman (1990) suggested a relationship of dry-rock Poisson's ratio to clay content. This was based on amplitude correlations of AVO models to seismic field CDP gathers.

Frequently, authors indicate that their empirical relationship is applicable to unconsolidated but not consolidated rocks, or the other way around. The significance of these statements can be understood by examining the limits of Gassmann's equation in Fig. 2.E.5.

Consolidated and unconsolidated rock examples are given in this figure. The analysis centers on the fact that Gassmann's equation can be separated into a dry-rock contribution and a pore-fluid contribution. Using the velocity and density values listed in the figure and Greenberg and Castagna's V_P-to-V_S relationship, Gassmann's equation was solved for the dry-rock and pore-fluid contributions. Two pore-fluid contributions are given: one for water saturation, the other for gas saturation. For the unconsolidated case, Gassmann's equation essentially tends toward the suspended-load model as suggested by Wood. The dry-rock contribution (1.63 GPa) is only 30% that of the contribution from the fluid (5.51 GPa). The choice of pore-fluid saturant dominates the value obtained for V_P. As Gregory noted, the choice of the dry-rock properties is not the most significant factor for unconsolidated rocks. However, the opposite is true for consolidated rocks. The pore-fluid contribution, be it water or gas, contributes little to the rock's total moduli. Accurate estimates of lithology and porosity are important when dealing with consolidated rocks.

These last two observations are reinforced by the graphs displayed in Figs 2.E.6 and 2.E.7. The change in V_P, V_S, and Poisson's ratio due to variations in porosity and water-saturation are shown for unconsolidated rocks and consolidated rocks. In Fig. 2.E.6, the left graph indicates a rapid and large decrease in V_P as the water saturation varies from 100% to 95%. This rapid decline was also previously depicted for the pore-fluid bulk modulus, K_{fl}, as a function of water saturation. This emphasizes the close correlation of V_P to pore-fluid properties for unconsolidated rocks. Since V_S is not that sensitive to pore-fluid content, Poisson's ratio correlates strongly to V_P.

Estimates of V_P and V_S for fluid substitution are fairly reliable if conventional well-log curves are provided. However, when porosity substitutions for the initial rock are

requested, then the results are not as reliable. Basically, if the porosity is changed, then the dry-rock moduli also have the opportunity to change in Gassmann's equation. As noted in the section on empirical relationships for velocity and density, there is a wide variance for unconsolidated and well-consolidated rocks.

For consolidated rocks (Fig. 2.E.7), the introduction of gas into the pores has little effect on V_P or Poisson's ratio. The change of porosity (or increase in fracture density) is more significant. This was noted in the bottom of Fig. 2.E.5 also.

In Figs. 2.E.6 and 2.E.7, it was assumed that the different fluids in the pore spaces were mixed at very fine scales. If the fluids are not well mixed with respect to the propagating wavelength, a patchy model is more appropriate for modeling the bulk modulus of the pore fluid rather than Wood's equation. The patchy model predicts a more linear drop in the fluid bulk modulus and thus in the *P*-wave velocity as the water saturation is varied. There are no abrupt changes in the *P*-wave velocity when 5% gas is introduced into a totally water-saturated rock. The current thought is that a patchy model is more appropriate for the sonic log response in hydrocarbon-charged formations, while Wood's model is more appropriate for the surface seismic. In short, sonic logs in gas zones can yield higher velocities than should be used in AVO modeling. Mavko et al. (1998) describe several patchy models for correcting sonic traveltimes for AVO modeling.

Fluid-Substitution Verification

Greenberg and Castagna (1992) verified their V_S estimation technique with measured laboratory data and well-log curves. The well-log verification is shown in Fig. 2.E.8. The correlation is excellent. In fact, it is difficult to see any separation between the dotted-curve (measured V_S) and the continuous curve (predicted V_S). However, the authors warned that the initial V_S estimate was not acceptable. A revised estimate of the lithology had to be conducted using sonic, neutron, and density curves to get the excellent match. The V_P values in the figure range from 10,000 to 16,000 ft (3000 to 5000 m)/s. These are consolidated rocks, and as noted, Gassmann's equation then requires an accurate lithologic estimate.

When a V_S curve is not available in a well, verification of the fluid-substitution technique can be preformed if two different pore fluids are present in the same formation. The well-log curves in Fig. 2.E.9 depict a thick sand zone that has three different pore-fluid states: gas, fizz, and water. The in-situ curves for the sonic, density, Poisson's ratio, and ln(acoustic impedance) are plotted in blue. The gas zone (8597-8630 ft) has low velocity, high resistivity, and neutron-density crossover. The fizz zone (8630-8670 ft) has a low velocity and a resistivity value slightly elevated over the water zone value (8670-8717 ft). The gas and fizz zones were replaced with water and the new rock properties are displayed by the red curves in the gas and fizz zones. Assuming that the only difference in the sand zone was the pore-fluid state, then the rock properties after fluid substitution to water should match the in-situ water-saturated rock properties. There is a good correlation.

Often a measured V_S log is "noisy" and questions are raised regarding whether it should be used for modeling. Fig. 2.E.10 shows measured and estimated curves for V_S and Poisson's ratio for a GOM deep-water well. The measured V_S curve (blue color)

has high-frequency variations that are not present on the other logs. The extreme values for these V_S fluctuations do not appear to be real. In situations such as this, the "good" zones of the measured V_S curve can be used to develop new regression coefficients for V_P-to-V_S transforms and then the estimated V_S is used for AVO modeling (Chesser, 1997).

Summary—Example of Fluid-Substitution Modeling

Numerous empirical and theoretical models have been described up to this point and the average reader should be swamped with thoughts such as "When to apply what." An example of a typical fluid substitution for AVO modeling should answer some of these questions.

Let's assume that a prospect has been defined near a well that has conventional well-log curves. Migrated CDP gathers have been obtained near the well and an AVO synthetic is desired to compare to the gathers. The well doesn't have hydrocarbons and an AVO synthetic is also desired to determine the seismic signature when various pore fluids are substituted for the in-situ brine. The petrophysical problem is to determine V_S for the in-situ AVO modeling and V_P, V_S, and ρ for the fluid-replacement AVO modeling.

The V_S prediction for the water-saturated in-situ rocks is simple, as illustrated in Fig. 2.E.11. The subscripts [,WET] and [,GAS] on the rock-property variables refer to the water-saturated and hydrocarbon-saturated states, respectively. Using the lithologic curves, the volume of each mineral component is determined at each depth point. The example rock is composed of 85% sand and 15% shale with an in-situ velocity of 11,400 ft (3500 m)/s. The simplest method of predicting V_S is by V_P-to-V_S transforms, such as those published by Greenberg and Castagna (1992). Once V_S is determined for the shale and sand components, the component velocities are averaged using the Voigt-Reuss-Hill effective-medium model. This procedure is repeated for the entire depth of the well. With V_P and density values taken from the in-situ logs and V_S predicted as shown, the in-situ AVO synthetic can now be generated.

The petrophysical work needed for fluid-substitution AVO modeling is covered in the next four figures. As shown in the upper portion of Fig. 2.E.12, porosity and density are additional parameters required for pore-fluid substitution. Of course, the desired S_W and the pore-fluid description (API, GOR, etc.) need to be defined.

The solution is broken into two parts. In the first part, (A), the elastic constants for the water-saturated rock are estimated and then these elastic constants are used in the second part (B) when new pore fluids are introduced. In Fig. 2.E.12, model equations and numeric values for estimating the bulk moduli of the total rock (K_{WET}), pore fluid ($K_{fl,WET}$), and minerals (K_{ma}) are given. For convenience in this example, the density and modulus for the pore fluid were taken from Domenico's table. However, it is recommended that Batzle-Wang's method of estimating the pore-fluid properties be followed. Domenico's values were derived for a specific set of environmental conditions (pressure and temperature gradients, specific gas density, salinity, etc.) and these conditions would normally not match other areas. Mavko et al. (1998) provided step-by-step numeric examples for calculating the pore-fluid properties with the Batzle-Wang equations.

The next step, shown in Fig. 2.E.13, contains the Greenberg-Castagna inversion of Gassmann's equation to find K_{dry}. The X, Y, and b shown in Part A.3 have no physical meaning; they are only intermediate variables to aid in the solution.

This is not the only technique for estimating K_{dry}. In Fig. 2.E.4, two other methods for obtaining K_{dry} were suggested. One is the Biot coefficient technique. If Biot's coefficient is approximated with one of the models described in Fig. 2.D.8, then $K_{dry} = (1-B)K_{ma}$. Remember B is based on the known porosity and K_{ma} has been determined in the previous figure. Now, the only variable that is unknown in Gassmann's equation for V_P is μ_{dry}. Once this is found, the new pore fluids can be introduced (following step A.4 in Fig. 2.E.13).

The other method suggested in Fig. 2.E.4 for estimating K_{dry} is to use the dry-rock Poisson's ratio. If this model is selected for providing additional information to Gassmann's equation, then a solution proposed by Gregory (1977) can be employed. Application of any of these three methods (Greenberg-Castagna, Biot's coefficient, or dry-rock Poisson's ratio) will supply the information listed in Fig. 2.E.13 at the end of Part A.3. The last portion for estimating the properties of the water-saturated rock is given in Part A.4 of Fig. 2.E.13.

The last petrophysical stage for AVO modeling with fluid-substitution properties is rather straightforward. The only additional rock properties needed, beyond what was calculated from the water-saturated case, are the hydrocarbon-charged values for the total rock density and the pore-fluid bulk modulus. Then the rock properties associated with the hydrocarbon-charged state are inserted into Gassmann's equation. These steps are worked out with numeric values in Figs. 2.E.14 and 2.E.15.

2F. Back to Geology through Anstey

With all the theoretical and empirical relationships presented in this section, the author seems to have lost sight of geologic processes. How does one return to the basics? There is no better way than through the geophysicist's own Shakespearean orator, Nigel Anstey. All geophysicists who have made Society presentations and also listened to one of Nigel's inspiring presentations develop a fear for the future. That fear is, "Oh Lord, please never make me follow Nigel in a technical presentation!"

Nigel gave such an illuminating presentation at Cambridge in 1990 that it was reproduced in *First Break*. After a few cartoons on squeezing and distorting the shape of a rock, it became obvious that a grain's shape and the number of contacts it has with other grains were going to be an important factor in predicting the *S*-wave velocity of the rock. Several of his intuitive observations are summarized in Fig. 2.F.1. His conclusions of the factors that control *S*-wave velocity were:

- First and foremost [is], probably, the cementation. Advanced cementation makes all rocks look much the same.
- But if there is no cementation, then [there are] those factors that control the number and angularity of the grain contacts—shape, then sorting, then overburden pressure.

- Now—where's lithology? Well, we will list it; the intrinsic rigidity of the grain material must be there, as must that of the cement. But not very clearly—partly because different lithologies often imply different angularity of the grain contacts, different natural cements, different susceptibility to pressure solution, different susceptibility to fracture, and so on ... [and] partly because the lithology becomes less important at porosities of reservoir quality.
- Then [there is] clay content—ranging from the low side of modest if the clay particles are just passengers in the pores, to the high side of modest if they are actually in the contacts. Then [there is] the saturant (just the minor effect of density), and the grain size (insofar as it controls the closing effect of overburden pressure, and preferential cementation).

Also noted was that porosity, as such, is not a major control on *S*-wave velocity.

But Nigel also wanted his conclusions to be phrased in terms that geologists know and understand, and this is accomplished as shown in the Fig. 2.F.2. The emphasis is that the number of grain contacts affects the rigidity of the rock. For fine-grained rocks, cement is likely to form preferentially in small pores and thus the rocks will have a higher rigidity than do coarse-grained rocks. Coarse-grained rocks that are well-rounded and well-sorted have fairly good porosity, and have many rigid contacts and thus a high shear-wave velocity for that porosity. This relates to the previous discussion on Han's observation of very-clean sand specimens. For angular-grained rocks, the sorting and packing, which can be related to geologic processes, control the number of contacts and thus the *S*-wave velocity.

While Anstey wanted to emphasize that examination of thin sections will provide insight into the geologic processes and thus predictions about the *S*-wave velocity, one has to wonder if these same predictions can be made from an interpretation based on seismic sequence stratigraphy.

Figures

Figure 2.A.1

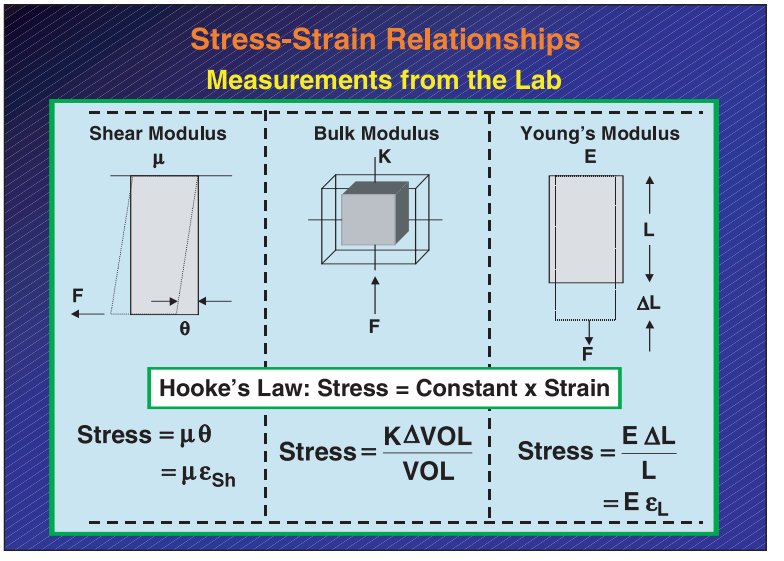

Figure 2.A.2

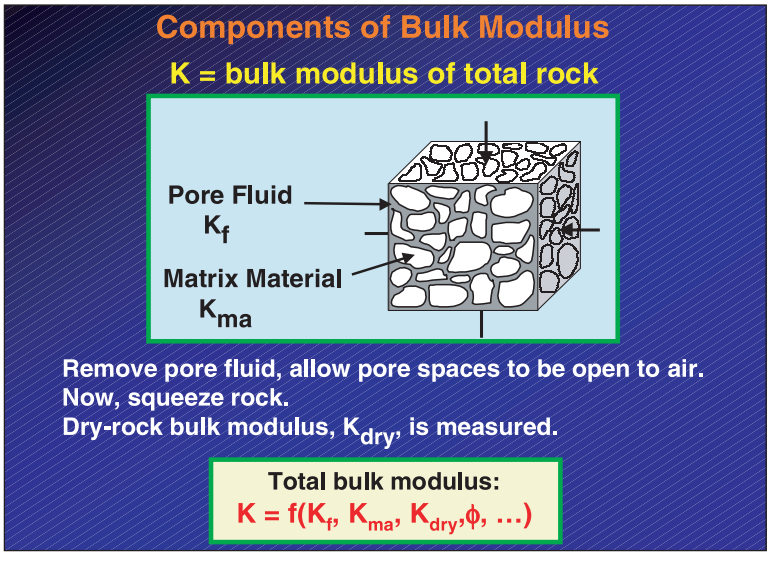

Figure 2.A.3

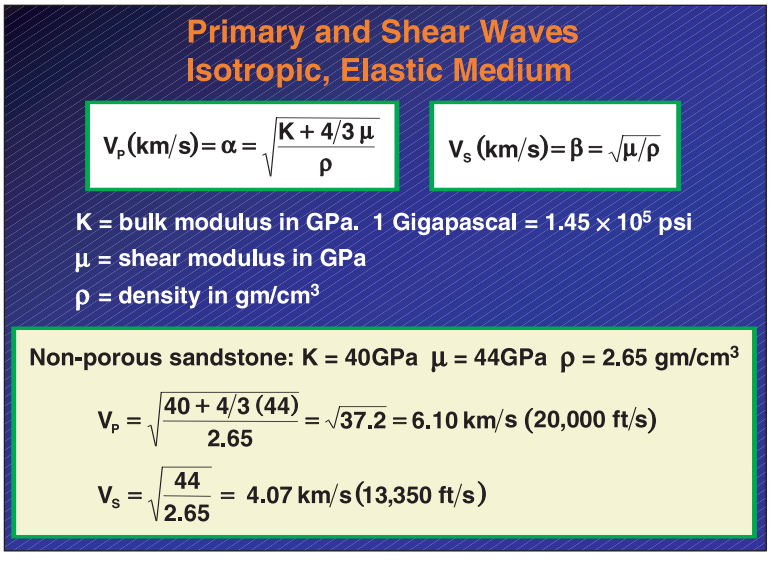

Figure 2.A.4

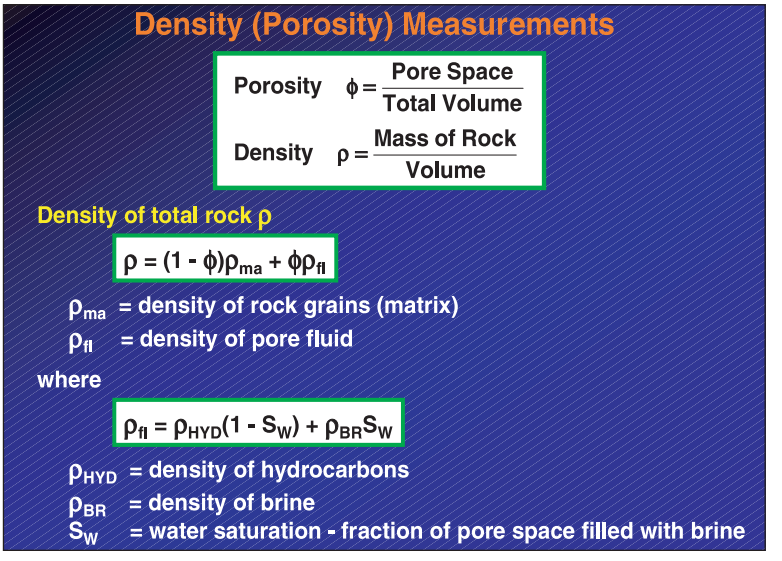

Figure 2.A.5

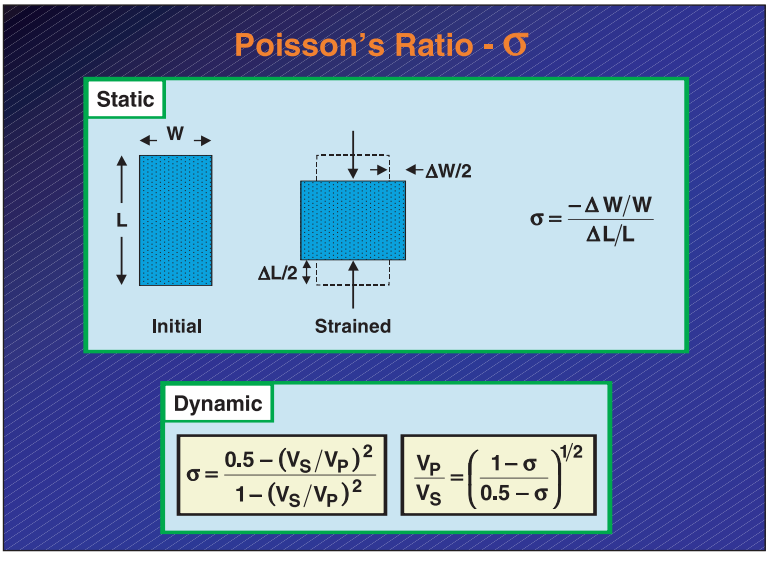

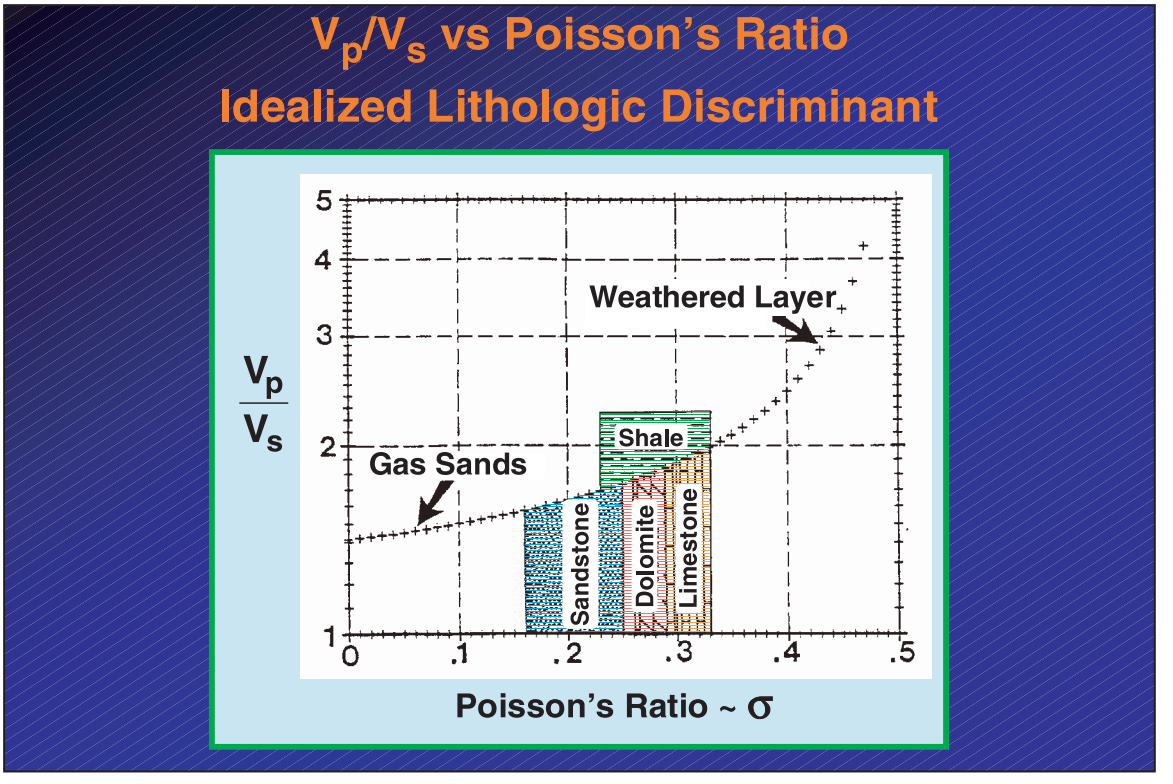

Figure 2.A.6

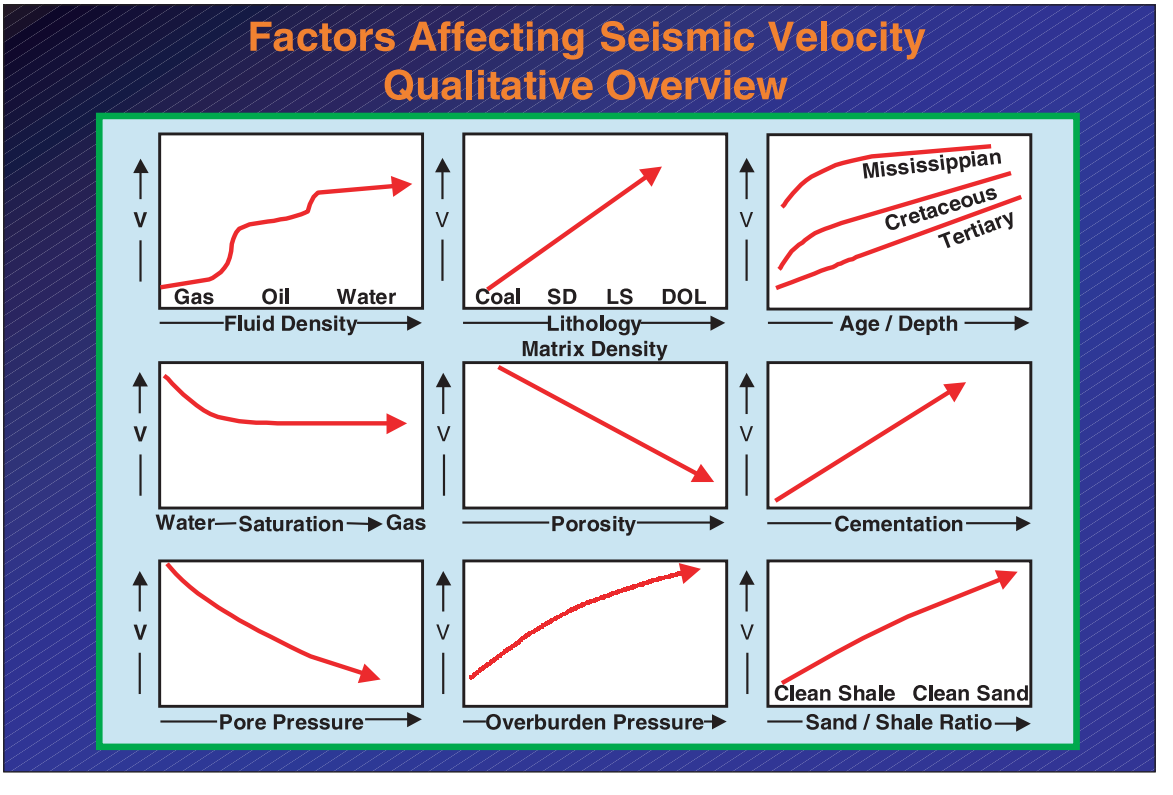

Figure 2.B.1

Figure 2.B.2

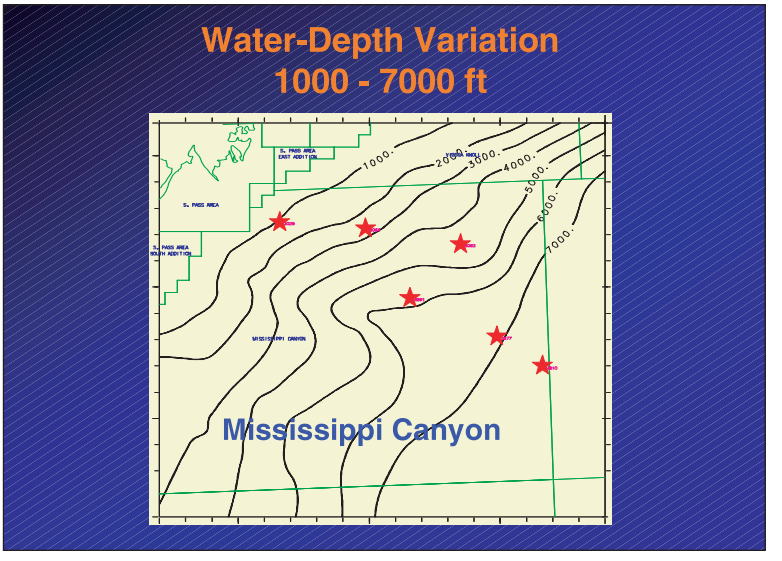

Figure 2.B.3

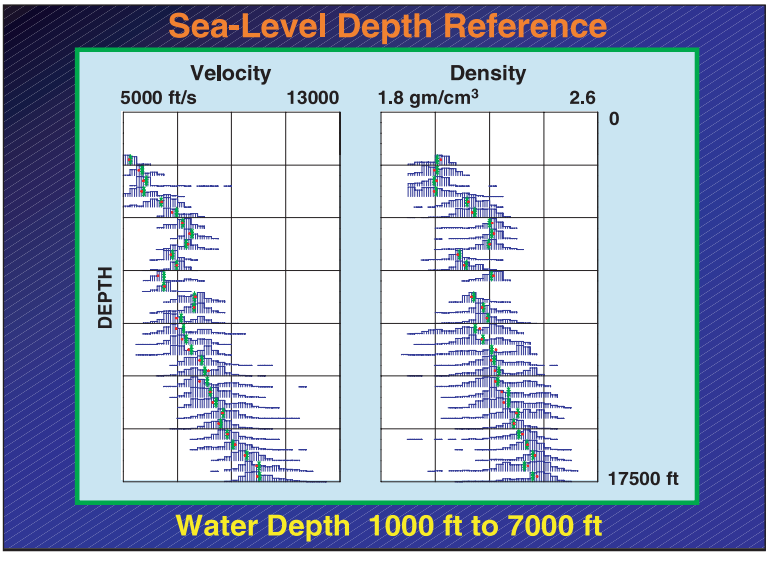

Figure 2.B.4

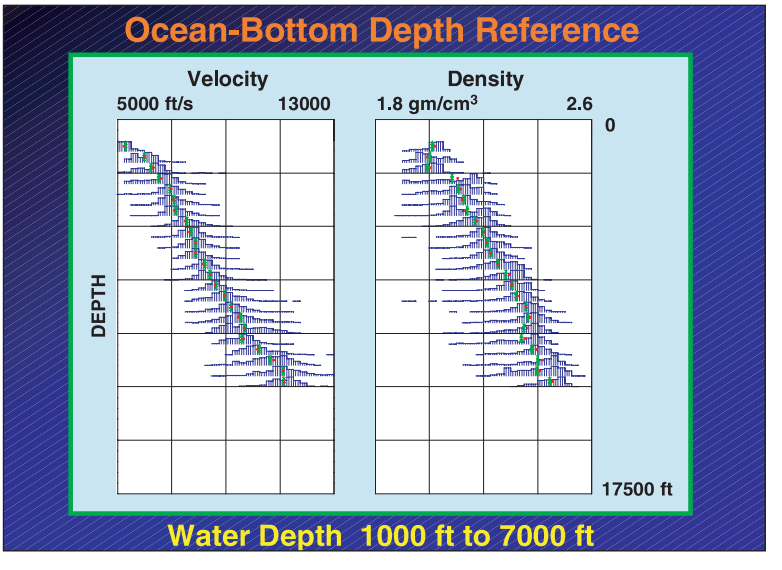

Figure 2.B.5

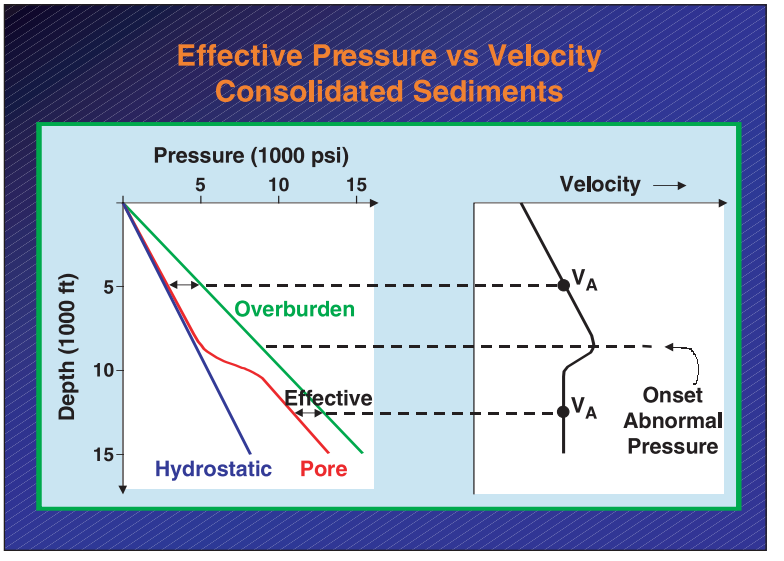

Figure 2.B.6

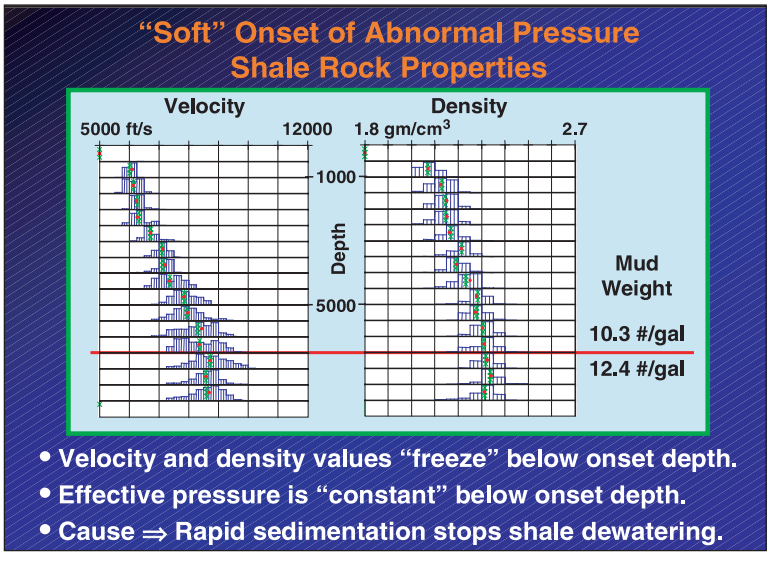

Figure 2.B.7

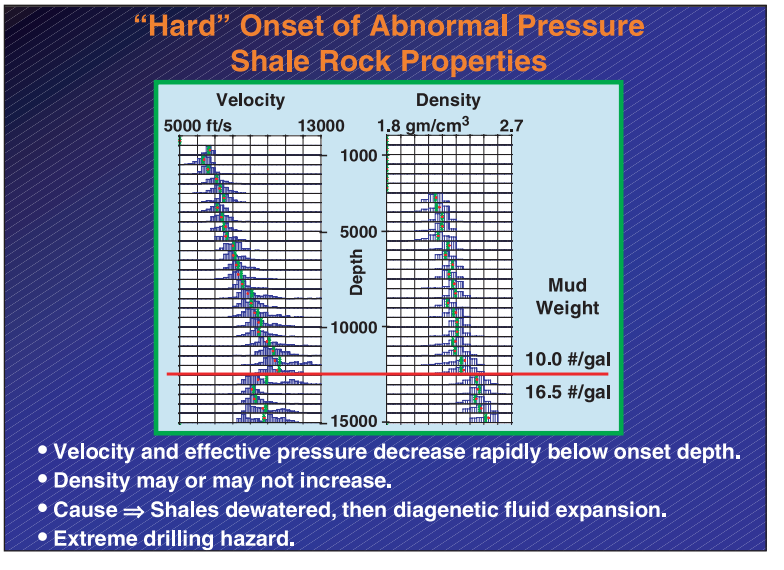

Figure 2.B.8

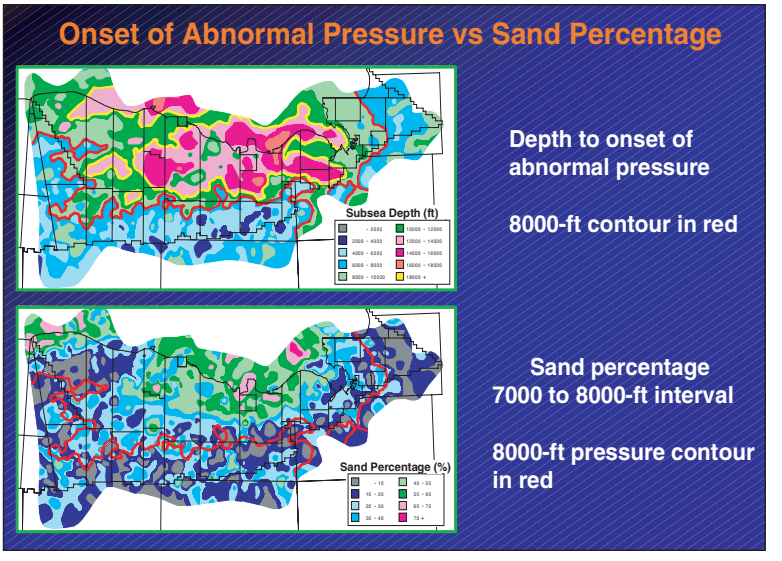

Figure 2.B.9

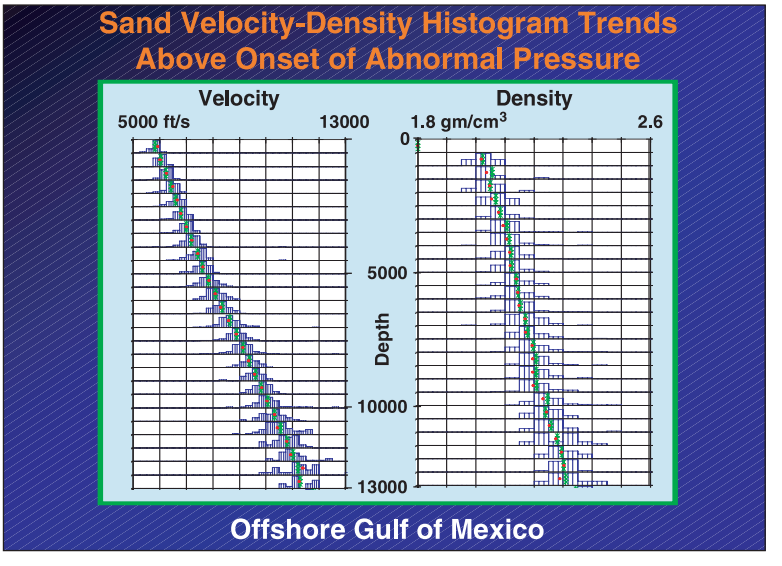

Figure 2.B.10

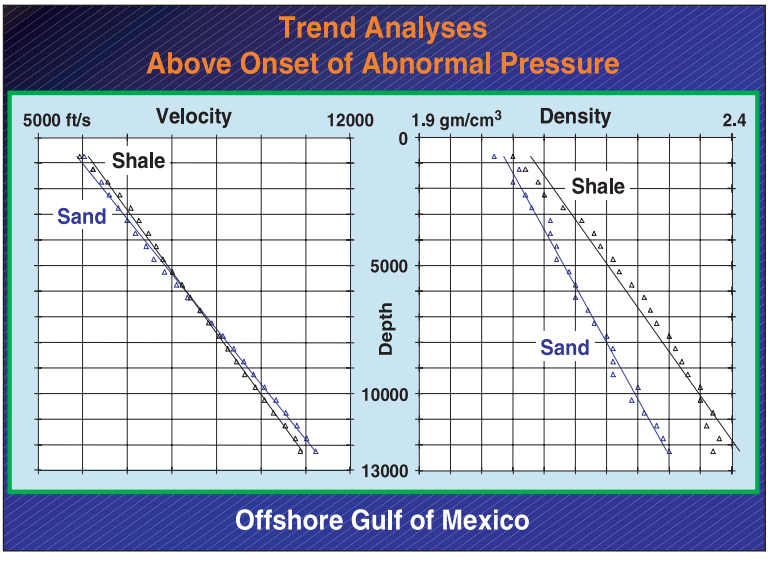

Figure 2.B.11

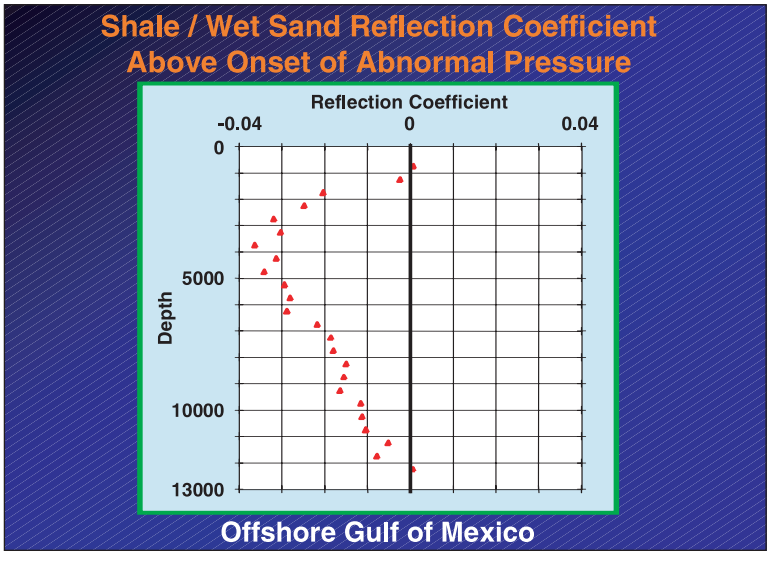

Figure 2.B.12

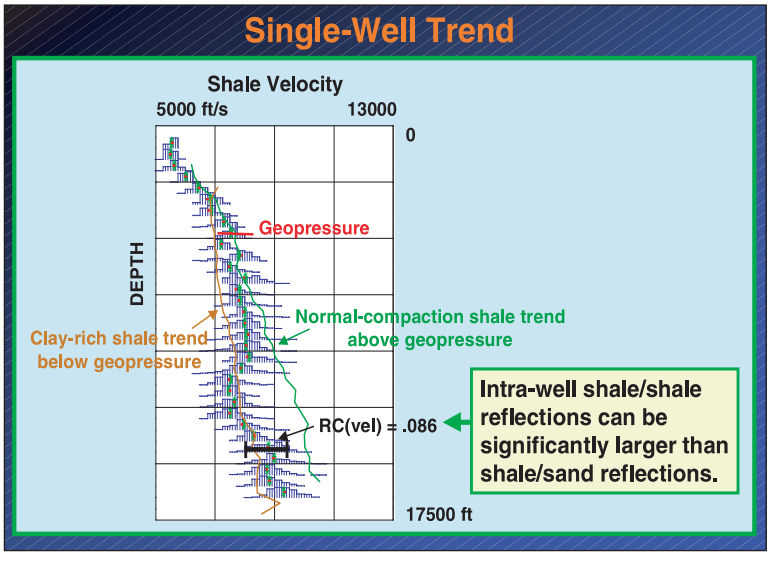

Figure 2.C.1

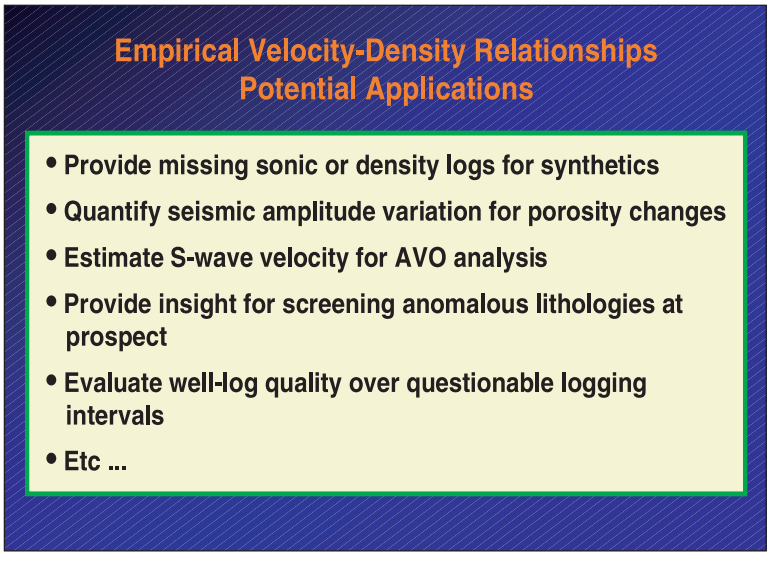

Figure 2.C.2

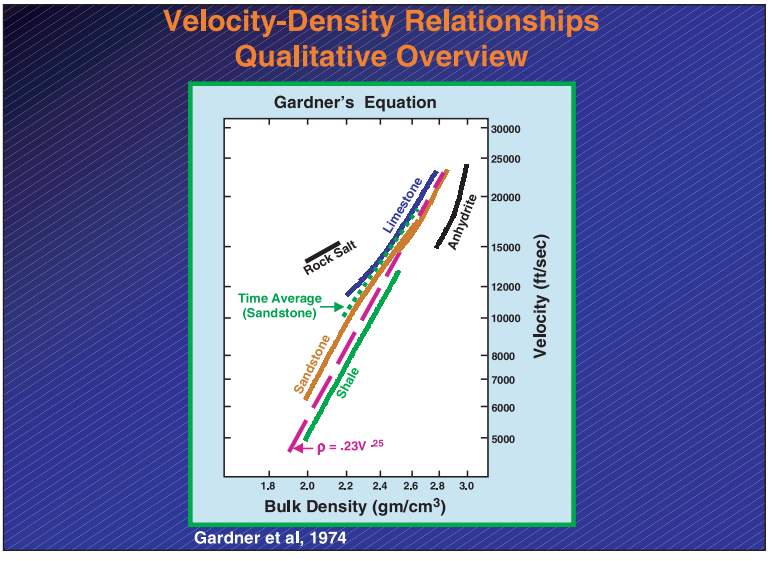

Figure 2.C.3

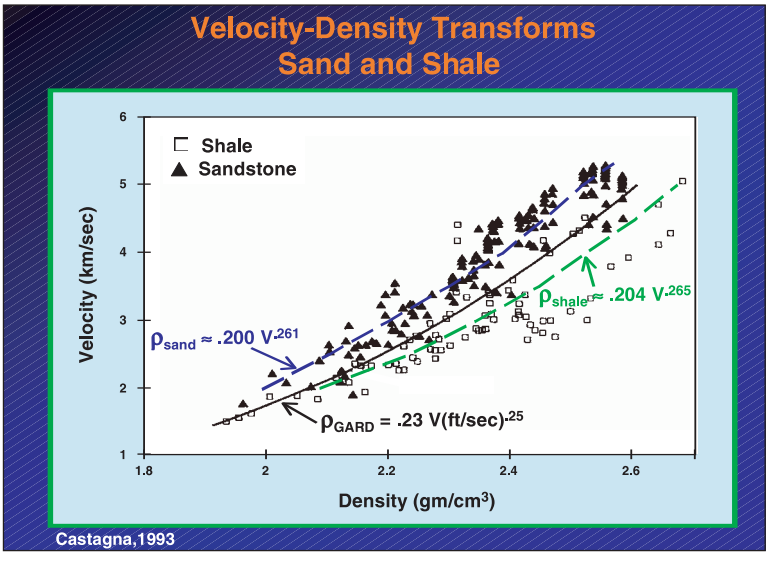

Figure 2.C.4

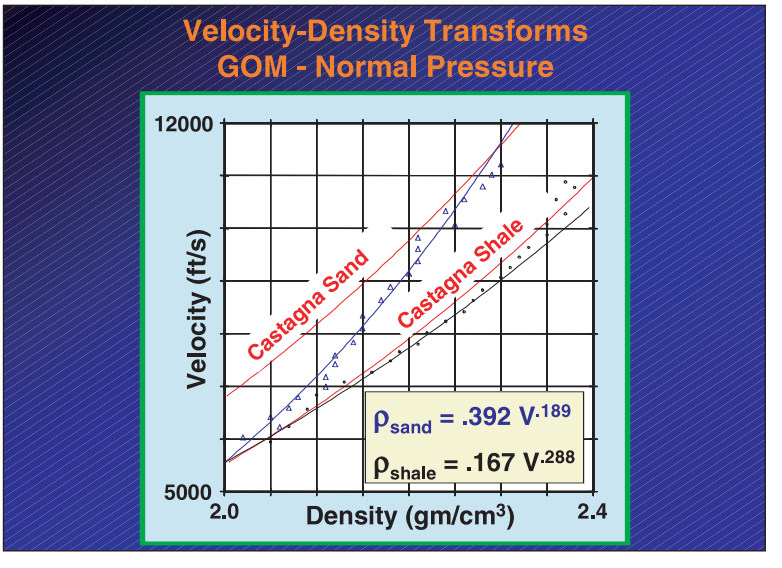

Figure 2.C.5

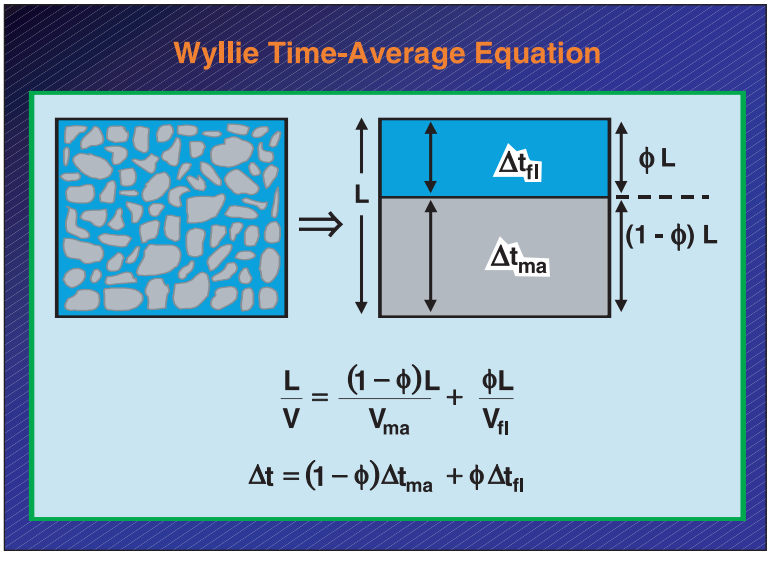

Figure 2.C.6

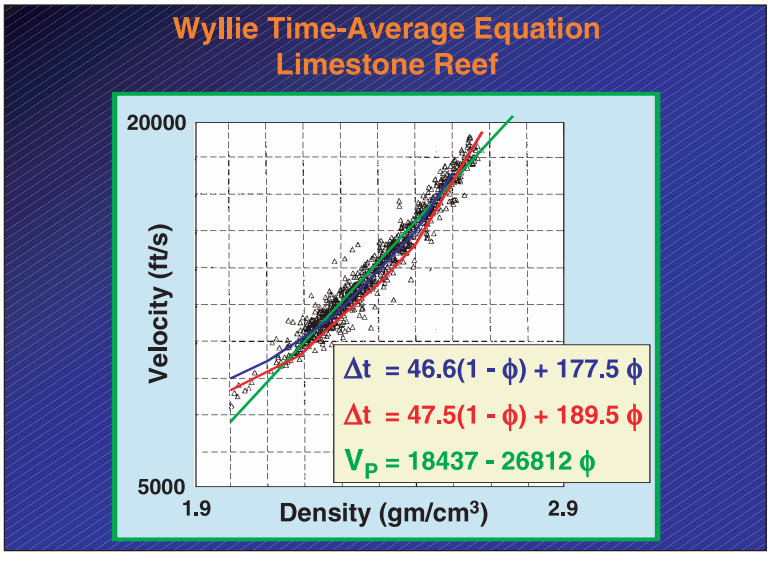

Figure 2.C.7

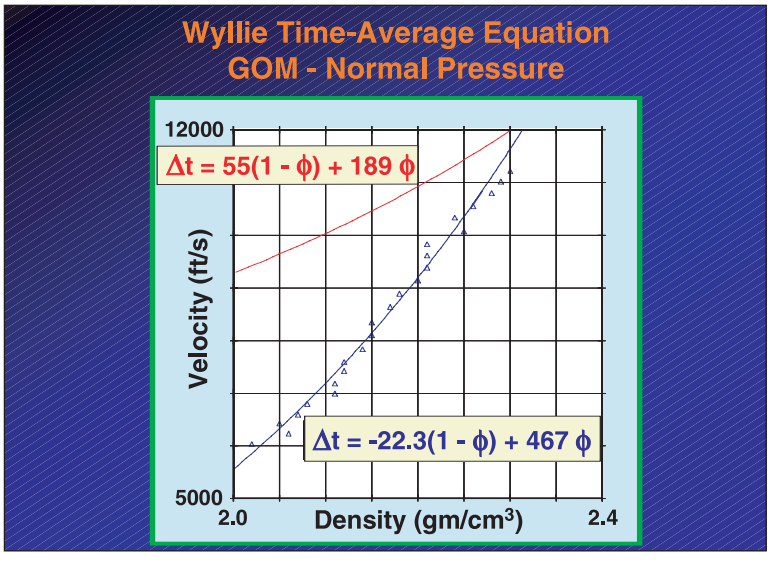

Figure 2.C.8

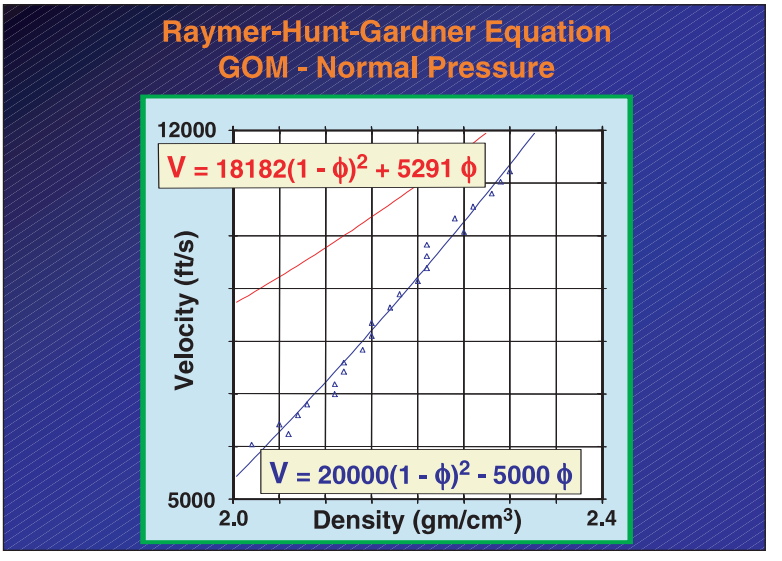

Figure 2.C.9

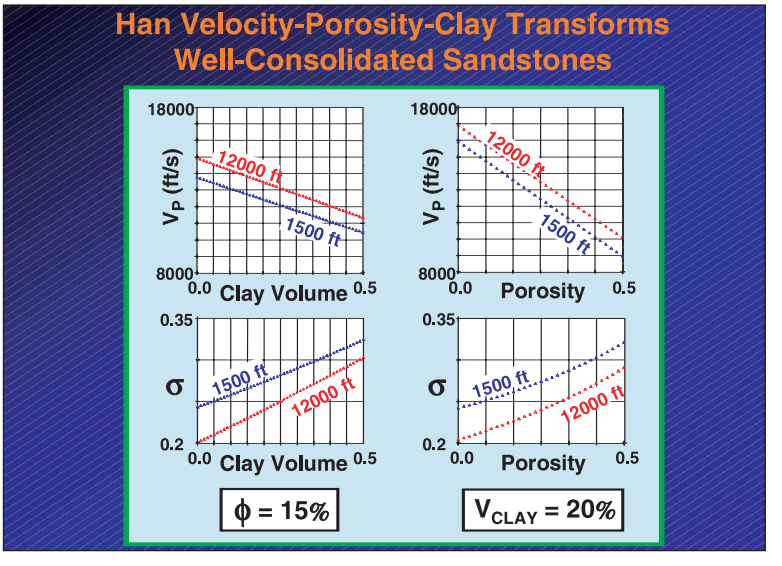

Figure 2.C.10

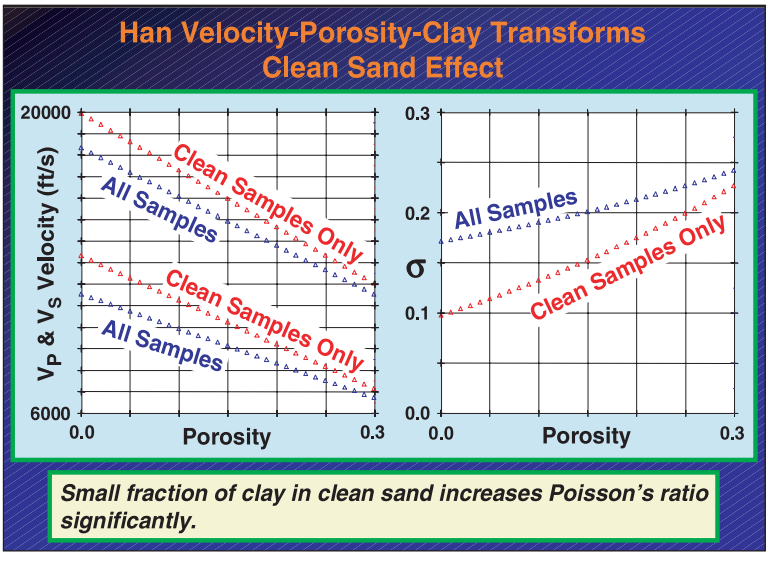

Figure 2.C.11

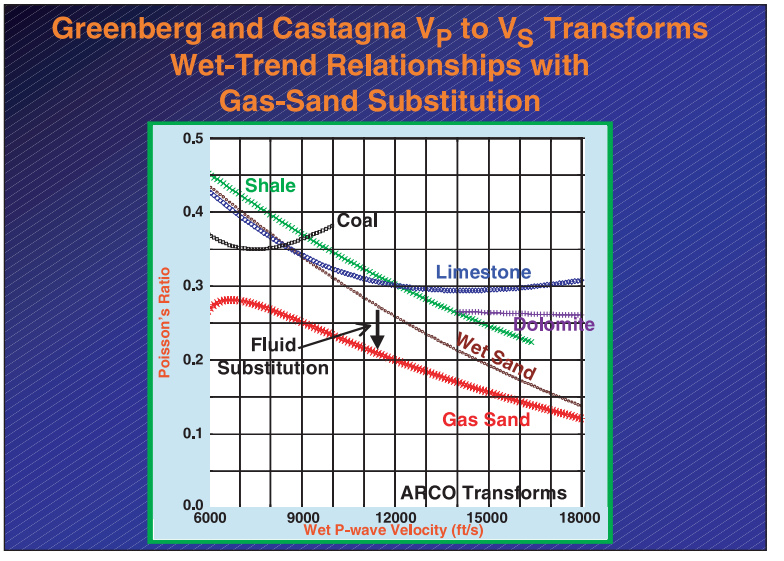

Figure 2.D.1

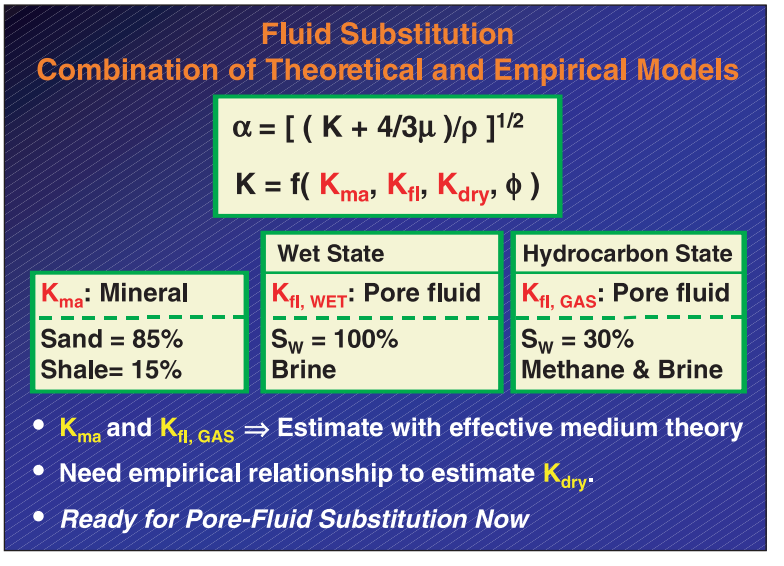

Figure 2.D.2

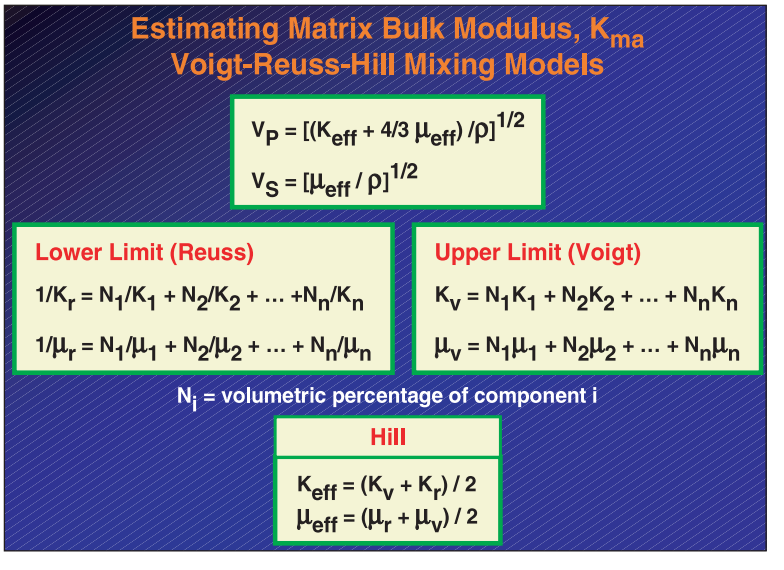

Figure 2.D.3

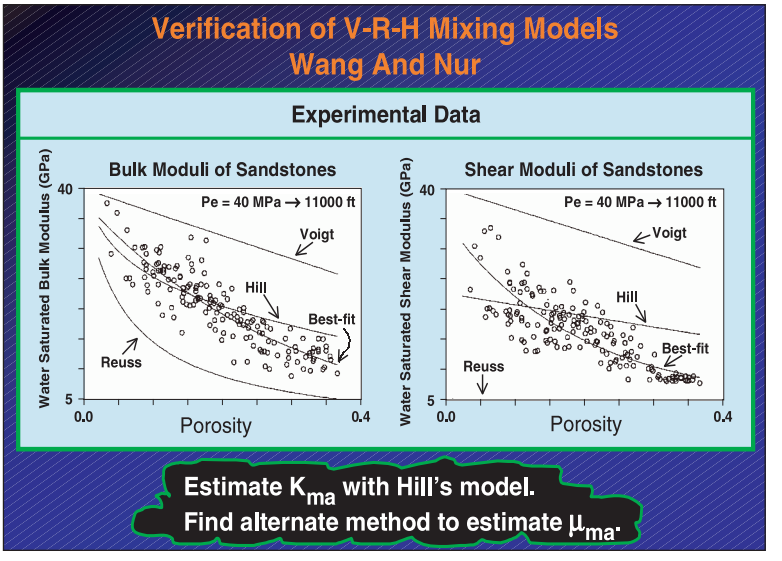

Figure 2.D.4

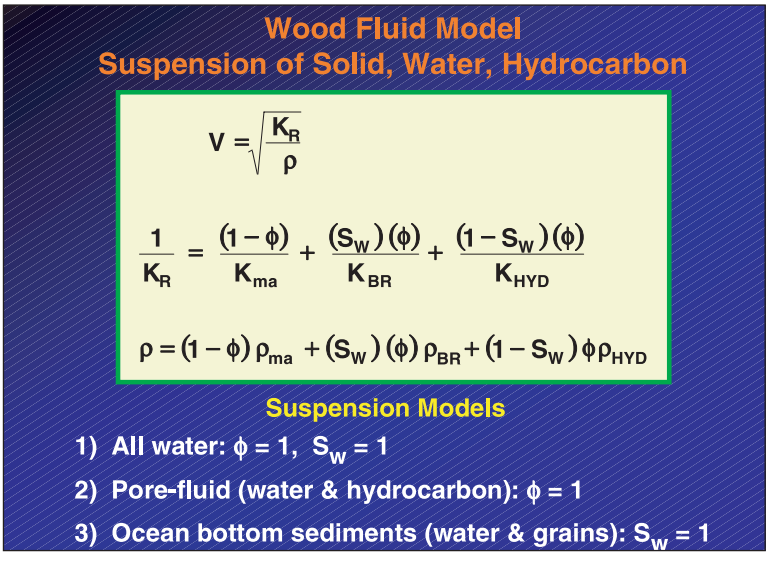

Figure 2.D.5

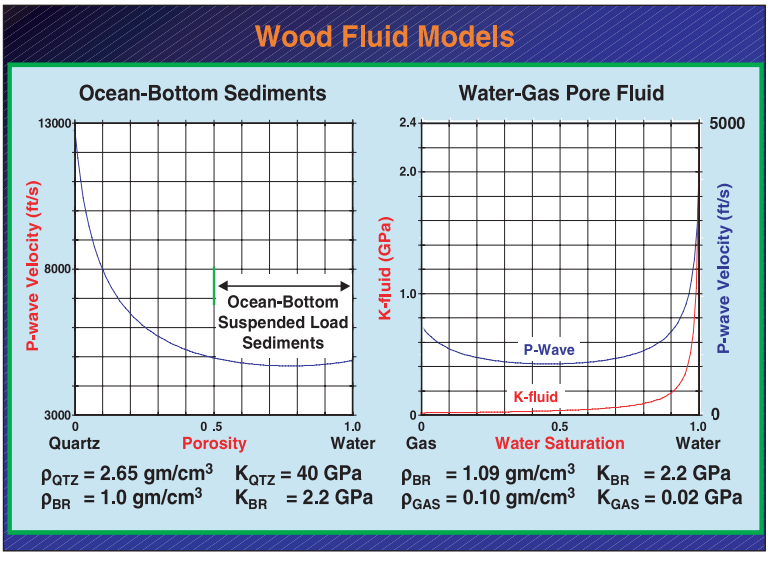

Figure 2.D.6

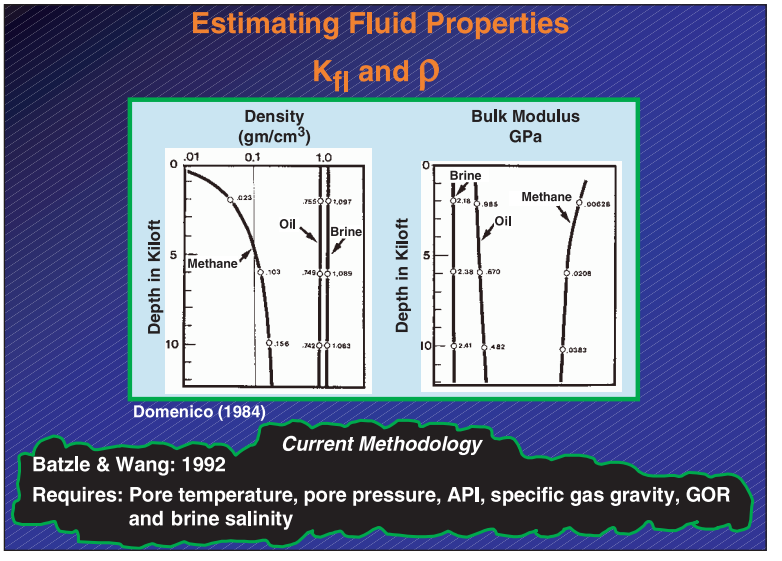

Figure 2.D.7

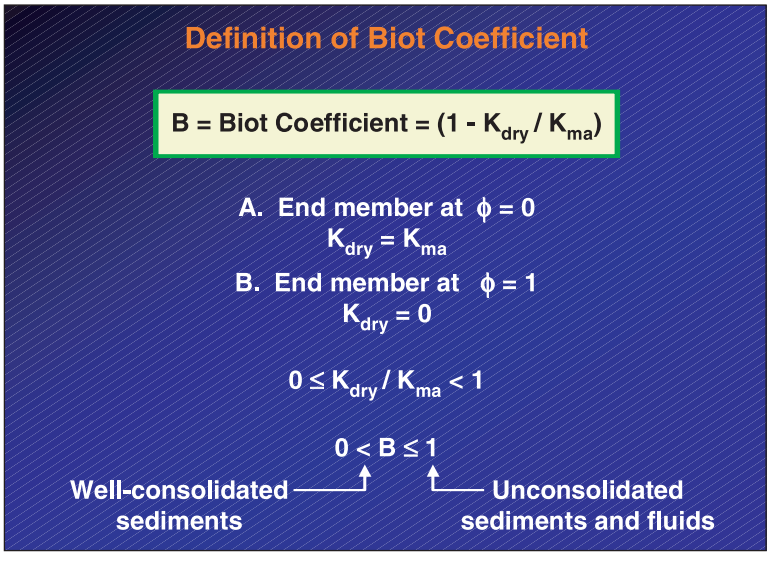

Figure 2.D.8

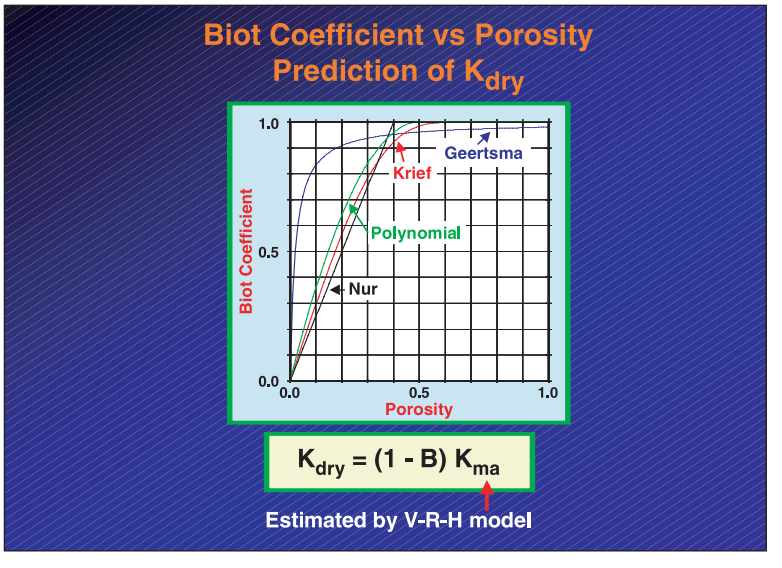

Figure 2.E.1

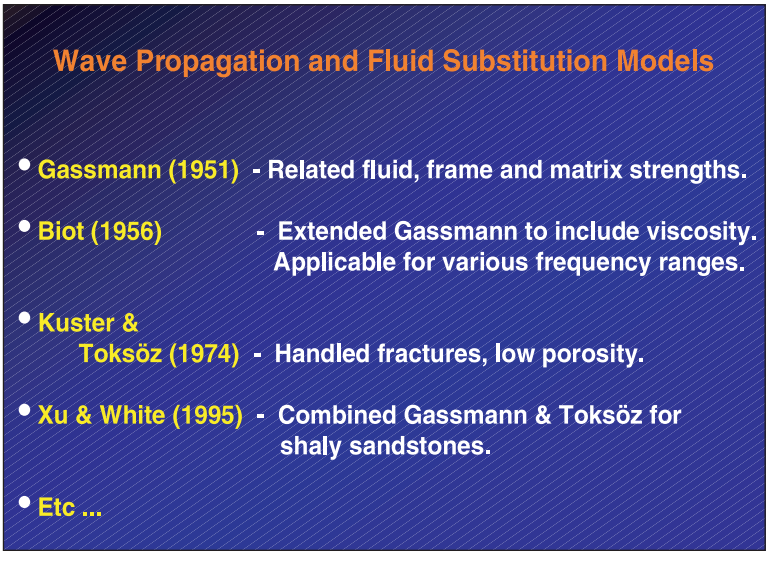

Figure 2.E.2

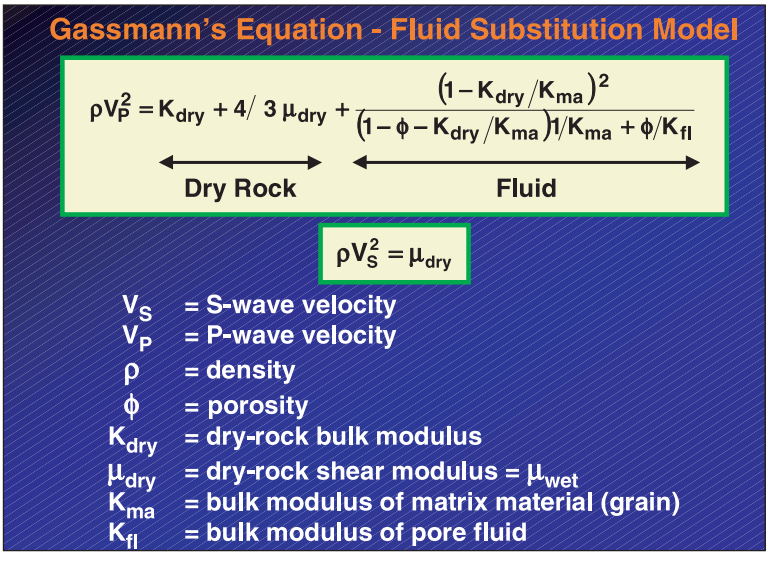

Figure 2.E.3

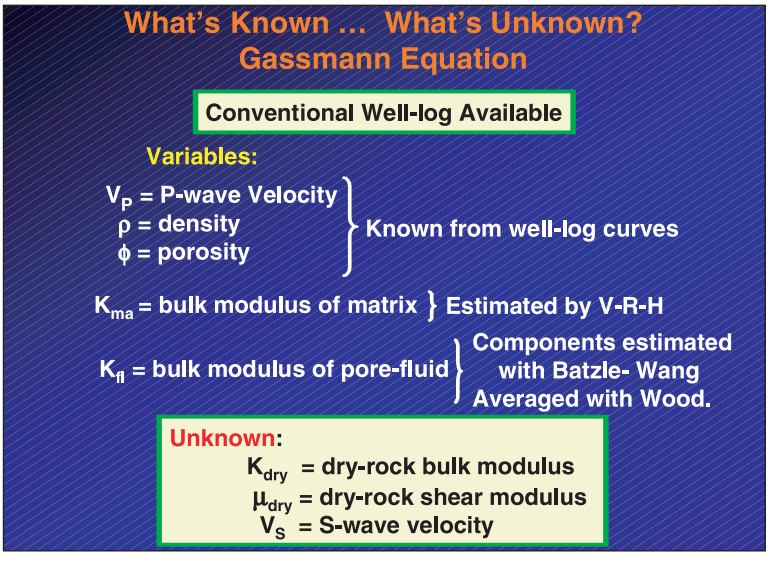

Figure 2.E.4

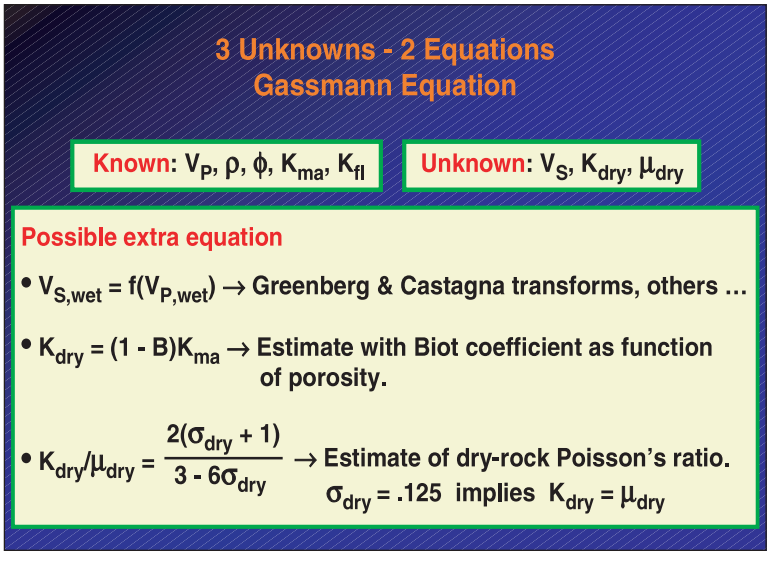

Figure 2.E.5

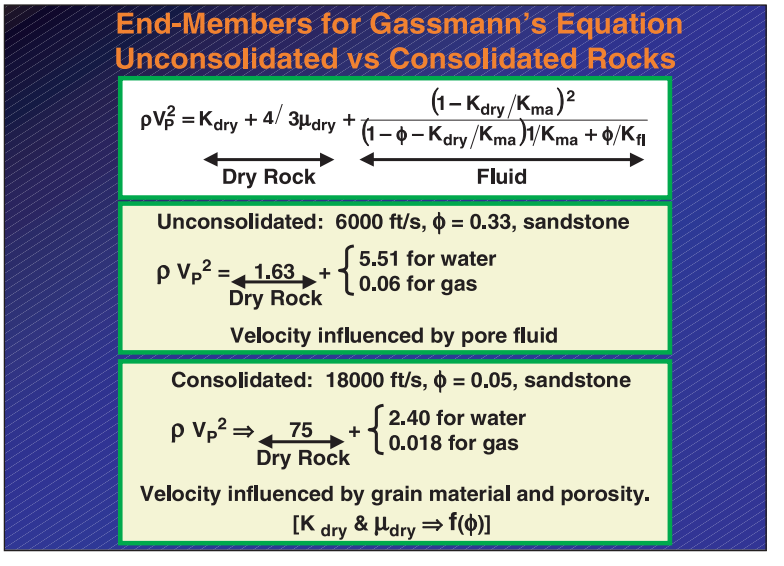

Figure 2.E.6

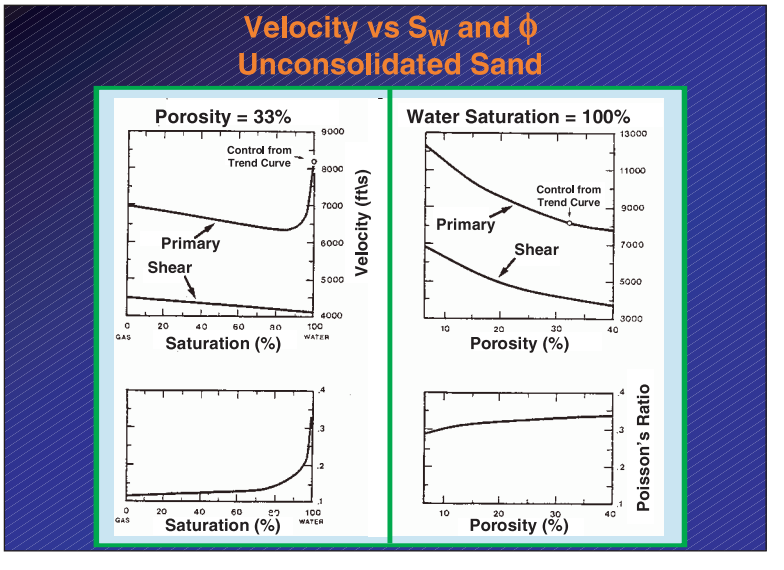

Figure 2.E.7

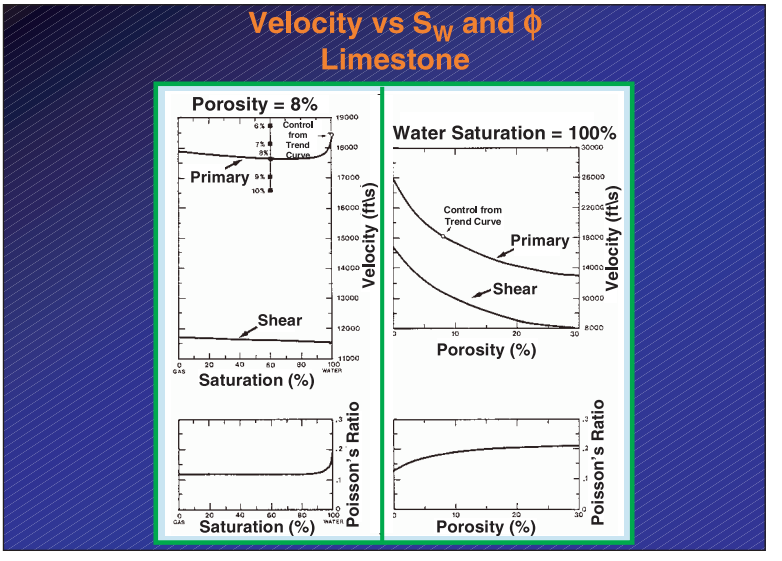

Figure 2.E.8

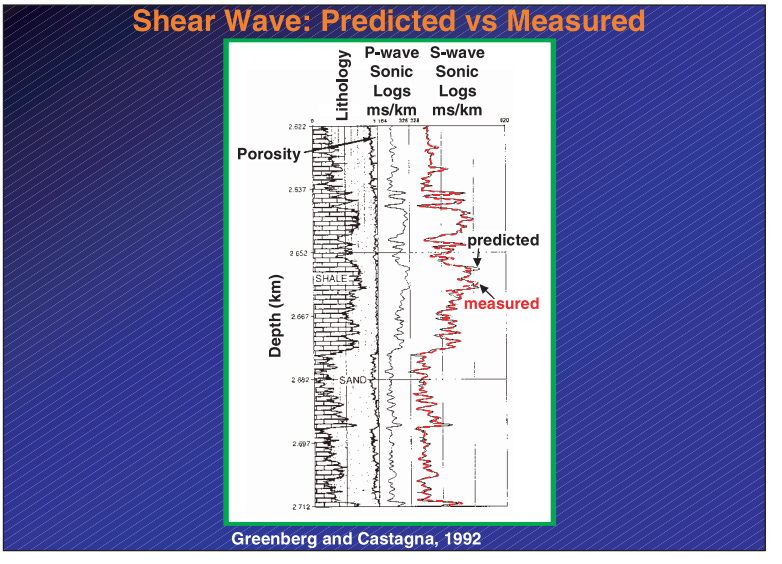

Figure 2.E.9

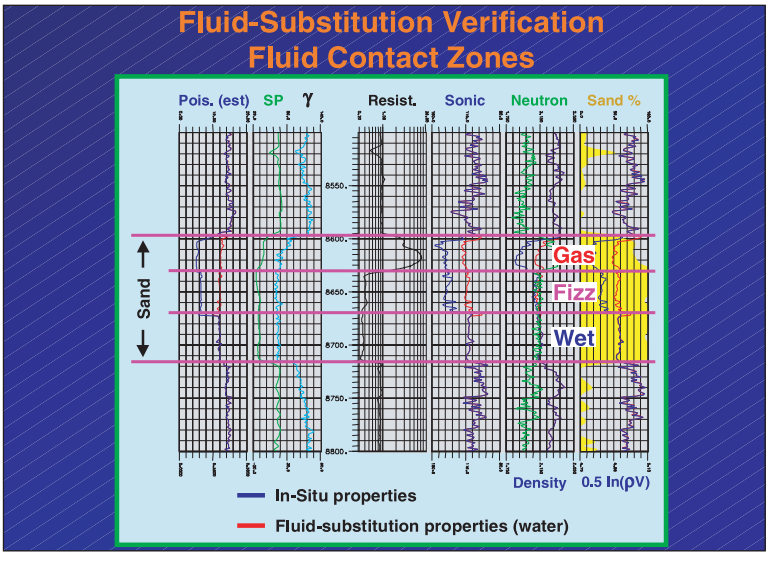

Figure 2.E.10

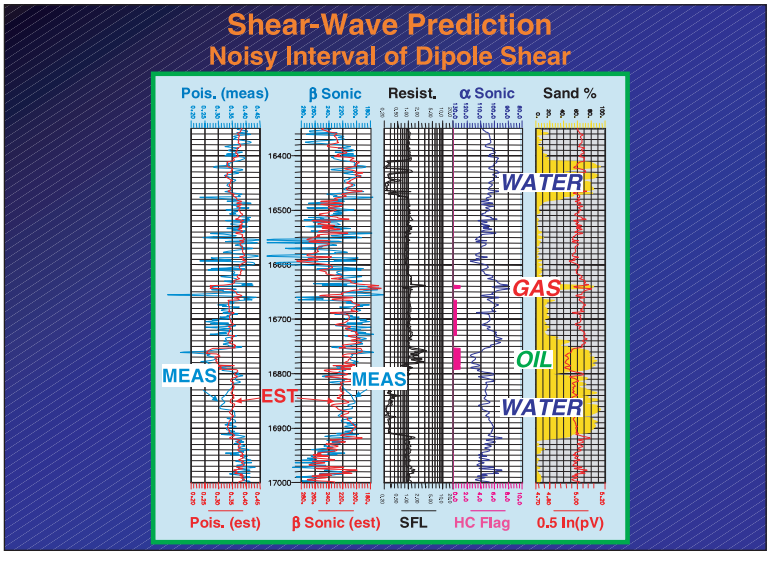

Figure 2.E.11

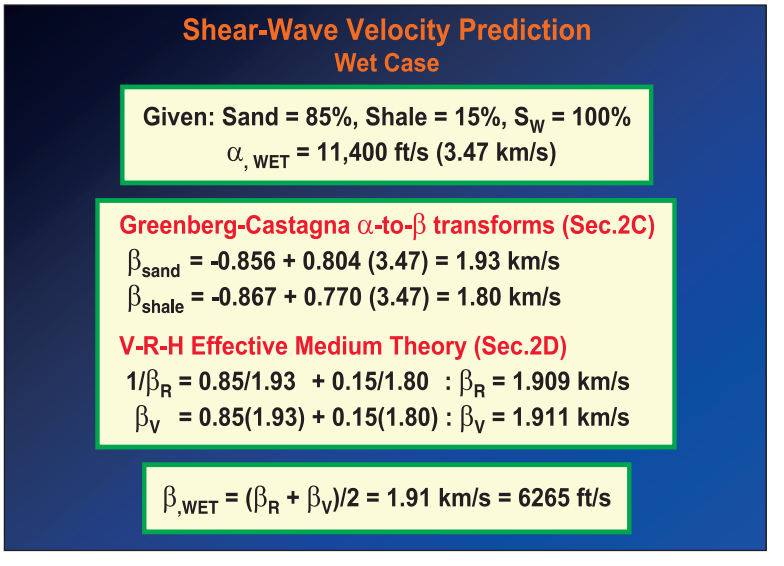

Figure 2.E.12

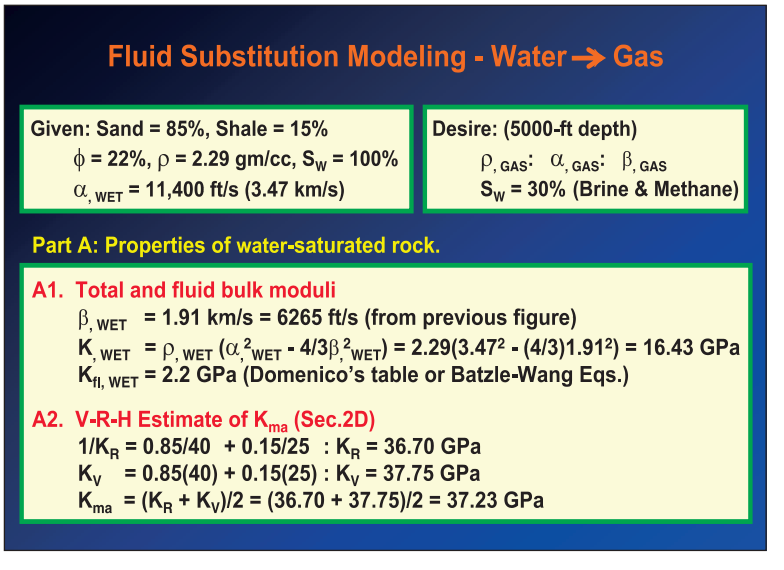

Figure 2.E.13

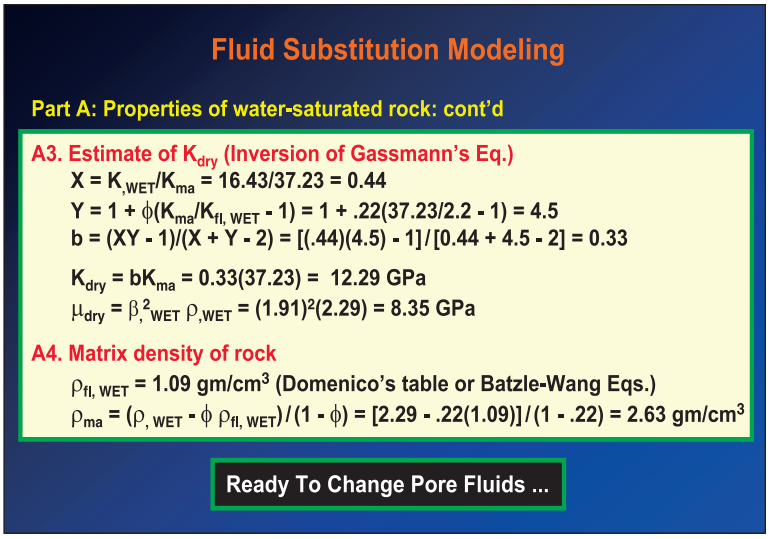

Figure 2.E.14

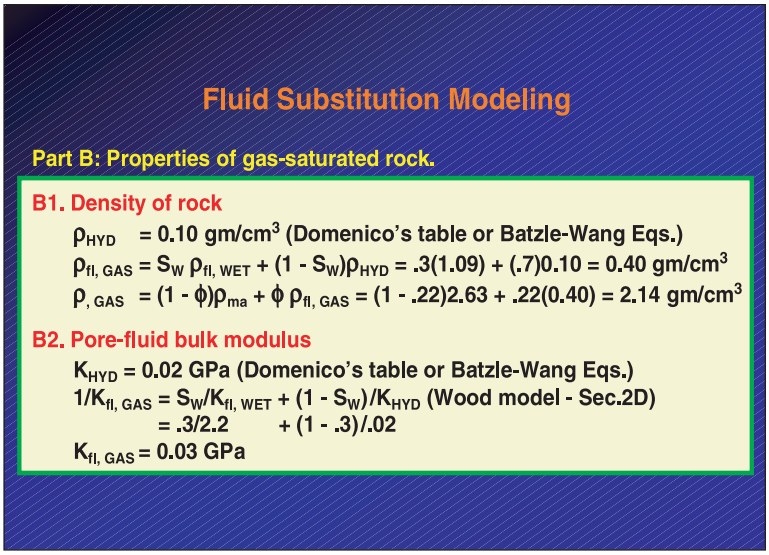

Figure 2.E.15

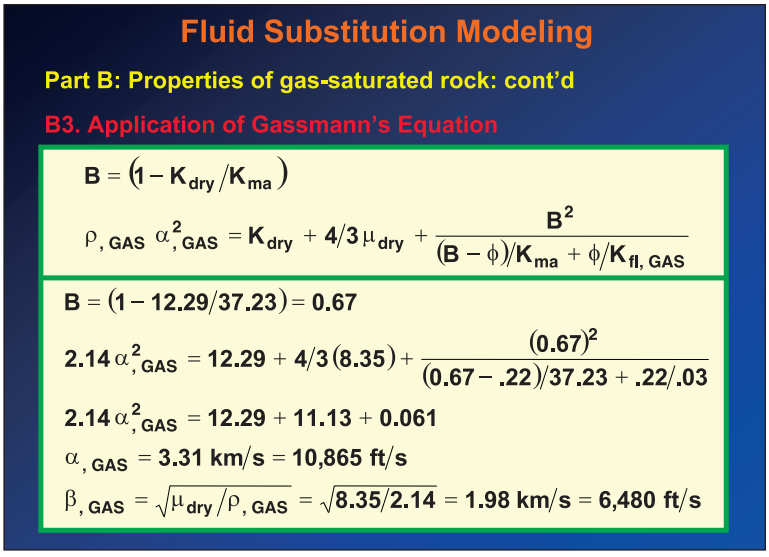

Figure 2.F.1

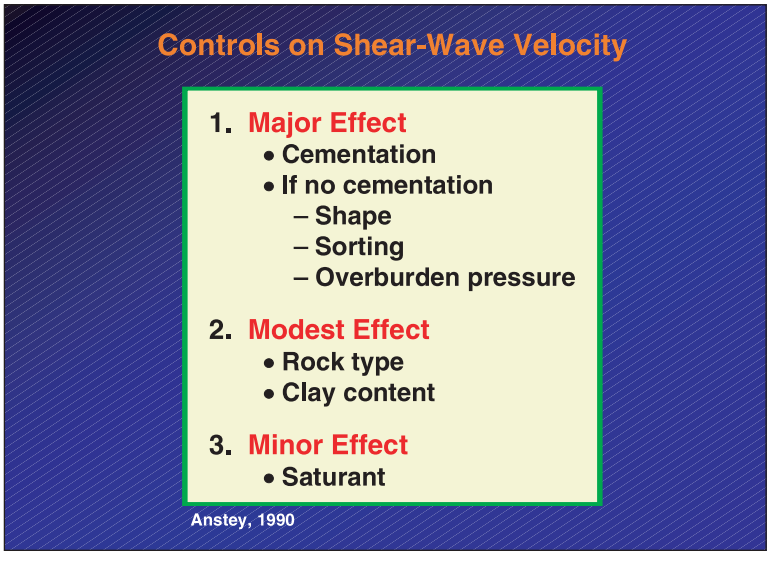

Figure 2.F.2